

The *TROY* project: II. Multi-technique constraints on exotrojans in nine planetary systems ★,★★,★★★

J. Lillo-Box¹, A. Leleu², H. Parviainen^{3,4,5}, P. Figueira^{1,6}, M. Mallonn⁷, A.C.M. Correia^{8,9,10}, N.C. Santos^{6,11},
P. Robutel⁸, M. Lendl¹², H.M.J. Boffin¹³, J.P. Faria^{6,11}, D. Barrado¹⁴, J. Neal^{6,11}

¹ European Southern Observatory (ESO), Alonso de Cordova 3107, Vitacura Casilla 19001, Santiago 19, Chile
e-mail: jlillobox@eso.org

² Physics Institute, Space Research and Planetary Sciences, Center for Space and Habitability - NCCR PlanetS, University of Bern,
Bern, Switzerland

³ Instituto de Astrofísica de Canarias (IAC), E-38200 La Laguna, Tenerife, Spain

⁴ Dept. Astrofísica, Universidad de La Laguna (ULL), E-38206 La Laguna, Tenerife, Spain

⁵ Sub-department of Astrophysics, Department of Physics, University of Oxford, Oxford, OX1 3RH, UK

⁶ Instituto de Astrofísica e Ciências do Espaço, Universidade do Porto, CAUP, Rua das Estrelas, PT4150-762 Porto, Portugal

⁷ Leibniz-Institut für Astrophysik Potsdam, An der Sternwarte 16, D-14482 Potsdam, Germany

⁸ IMCCE, Observatoire de Paris - PSL Research University, UPMC Univ. Paris 06, Univ. Lille 1, CNRS, 77 Avenue Denfert-
Rochereau, 75014 Paris, France

⁹ Department of Physics, University of Coimbra, 3004-516 Coimbra, Portugal

¹⁰ CIDMA, Departamento de Física, Universidade de Aveiro, Campus de Santiago, 3810-193 Aveiro, Portugal

¹¹ Departamento de Física e Astronomia, Faculdade de Ciências, Universidade do Porto, Portugal

¹² Space Research Institute, Austrian Academy of Sciences, Schmiedlstr. 6, 8042 Graz, Austria

¹³ ESO, Karl Schwarzschild Strasse 2, 85748 Garching, Germany

¹⁴ Depto. de Astrofísica, Centro de Astrobiología (CSIC-INTA), ESAC campus 28692 Villanueva de la Cañada (Madrid), Spain

In preparation

ABSTRACT

Context. Co-orbital bodies are the byproduct of planet formation and evolution, as we know from the Solar System. Although planet-size co-orbitals do not exist in our planetary system, dynamical studies show that they can remain stable for long periods of time in the gravitational well of massive planets. Should they exist, their detection is feasible with the current instrumentation.

Aims. In this paper, we present new ground-based observations searching for these bodies co-orbiting with nine close-in ($P < 5$ days) planets, using different observing techniques. The combination of all of them allows us to restrict the parameter space of any possible trojan in the system.

Methods. We use multi-technique observations (radial velocity, precision photometry and transit timing variations), both newly acquired in the context of the *TROY* project and publicly available, to constrain the presence of planet-size trojans in the Lagrangian points of nine known exoplanets.

Results. We find no clear evidence of trojans in these nine systems through any of the techniques used down to the precision of the observations. However, this allows us to constrain the presence of any potential trojan in the system, specially in the trojan mass/radius versus libration amplitude plane. In particular, we can set upper mass limits in the super-Earth mass regime for six of the studied systems.

Key words. Planets and satellites: gaseous planets, fundamental parameters; Techniques: radial velocity, transits; Minor planets, asteroids: general

1. Introduction

The development of state-of-the-art instrumentation and space-based facilities in the past decades boosted the discovery of extrasolar planets up to several thousands of detections¹. This

* Based on observations collected at the Centro Astronómico Hispano Alemán (CAHA) at Calar Alto, operated jointly by the Max-Planck Institut für Astronomie and the Instituto de Astrofísica de Andalucía (CSIC).

** Partly based on data obtained with the STELLA robotic telescopes in Tenerife, an AIP facility jointly operated by AIP and IAC.

*** Based on observations collected at the European Organisation for Astronomical Research in the Southern Hemisphere under ESO programmes 297.C-5051, 098.C-0440(A), and 298.C-5009

¹ <http://exoplanet.eu>

plethora has shown the wide diversity of intrinsic and orbital properties that planets can have. Exoplanet research is currently focused on the deep understanding of the planet composition, structure and atmosphere, in parallel to the search for Earth analogues. From our own system, we know that extrasolar systems should also host other components that also played an important role in moulding the architecture and properties of the planets. In the Solar System, moons and more recently trojans (e.g., Lucy mission, Levison et al. 2017) are targets for *in situ* exploration since they contain clues on the formation and early evolution of our planetary system (e.g., Morbidelli et al. 2005; Borisov et al. 2017).

Trojan bodies co-rotate with planets in a wide variety of orbital configurations, mainly in tadpole (orbiting the gravity

wells of the L_4 and L_5 Lagrangian points) and horseshoe (librating from L_4 to L_5 in a horseshoe-like orbit in the co-rotating frame) orbits (see, e.g., Laughlin & Chambers 2002). The formation of these bodies is still under debate and two main mechanisms are proposed. First, in the *in situ* formation scenario, these bodies would form in the Lagrangian points throughout multiple inelastic collisions between the remnant dust particles of the protoplanetary disk trapped in the gravitationally stable regions. Indeed, swarms of particles trapped in the Lagrangian points are common outcomes of the hydrodynamical simulations used to explain the features observed in transition disks with potentially forming planets (e.g., Fuente et al. 2017; Laughlin et al. 2002). Similarly to the core accretion process, this trapped material could have grown to larger bodies from kilometer- to moon- or planet-size by particles and pebble collisions. Interestingly, Beaugé et al. (2007) demonstrate that co-orbital bodies up to 6 times the mass of Mars can be formed in these regions under certain conditions and remain in stable orbits. Another proposed mechanism is the capture of these bodies in the Lagrangian points of giant planets during their migration along the disk (see, e.g., Namouni & Morais 2017). This would allow larger bodies to be trapped in these regions. Each of these mechanisms, occurring during the first stages of the planet formation and evolution processes, have different imprints in the physical and orbital properties of the co-orbitals. Hence, they contain primordial information about these first stages of the system. Consequently, the study of trojans in the Solar System and the search for trojans in extrasolar systems (and minor bodies in general, Lillo-Box et al. 2018b) is key to understand the whole picture of the properties of planetary systems. In particular they can provide significant insight into the nature of formation processes by allowing us to understand if some exoplanetary properties, like the presence of Hot Jupiters, are a product of nature (formation) or nurture (evolution).

Previous works have developed different techniques to search for these bodies but none has been found yet. Several techniques have been explored, namely radial velocity (Ford & Gaudi 2006; Leleu et al. 2015, 2017), transits (Janson 2013; Hippke & Angerhausen 2015), or transit timing variations of the planet (Ford & Holman 2007; Madhusudhan & Winn 2009; Schwarz et al. 2016). In Lillo-Box et al. (2018a), we presented the *TROY* project, a multi-technique effort to detect the first bodies co-orbiting to known extrasolar planets. We analyzed a combination of radial velocity and transit data with the methodology described in Leleu et al. (2017) (a generalization of the Ford & Gaudi 2006 technique, expanding the parameter space to horseshoe and large amplitude tadpole orbits). We used archive radial velocity data together with Kepler and ground-based light curves to constrain exotrojan masses in 46 single-planet systems in short-period orbits ($P < 5$ days). We found no significant evidence of trojan bodies in any of the studied systems, but we could place upper limits to masses in both Lagrangian points and start populating the parameter space towards a definition of the trojan occurrence rate at different mass regimes. For instance, we could discard Jupiter-mass (or more massive) trojans in 90% of the systems, which might indicate difficulties in forming, capturing, or keeping trojans in stable orbits during the inward migration of the planet (as theoretically predicted in, e.g., Rodríguez et al. 2013).

Some of the systems studied in Lillo-Box et al. (2018a) show hints for a mass imbalance between the two Lagrangian points, at the 2σ level. Despite not being significant detections, they certainly deserve additional follow-up. In this paper we present an extensive amount of dedicated radial velocity and light curve

data of nine of these systems to look for the planet-mass co-orbital candidates found in our previous work. In Section 2 we describe the multi-technique observations and data reduction. In Section 3 we present the methodology followed to constrain the different regions of the parameter space to restrict the possible presence of trojan planets in these systems; and Section 4 present the results for each individual system. In Section 5 we discuss these results. In Appendix A and B we show the large figures and long tables (respectively).

2. Observations

We have used several datasets from previous publications as well as newly acquired data. In this section we summarize these observations and briefly describe the target sample.

2.1. Target sample

Nine systems were selected for further follow-up from our radial velocity analysis in Lillo-Box et al. (2018a) because they presented hints for some mass imbalance between the two Lagrangian points. The selected systems are shown in the first column of Table 1. The planets in all nine systems studied here have been confirmed and characterized through both transits and radial velocity observations. Among them, seven are gas giants with masses above one Jupiter mass, HAT-P-12 b is a Saturn-mass planet, and GJ 3470 b is a $13.7 M_{\oplus}$ planet. All of them transit main-sequence stars of spectral types FGK (and M in the case of GJ 3470) with orbital periods below 3.5 days.

2.2. Radial velocity

We used the archive radial velocity data presented in Lillo-Box et al. (2018a) and newly acquired high-resolution spectra from HARPS (Mayor et al. 2003), HARPS-N (Cosentino et al. 2012) and CARMENES (Quirrenbach et al. 2014). In Table 1 we present a summary of the new radial velocity observations obtained for each of the nine systems, distinguishing between archive and new observations.

All three instruments are high-resolution fiber-fed échelle spectrographs with resolving powers $R = 120\,000$ (HARPS, 3.6 m telescope at La Silla Observatory, ESO, Chile), $R = 120\,000$ (HARPS-N, TNG telescope at ORM observatory, La Palma, Spain), and $R = 81\,200$ (CARMENES, 3.5 m telescope at Calar Alto Observatory, Almería, Spain). These instruments are all located in temperature and pressure controlled vacuum vessels inside isolated chambers to improve their stability. Also, all three instruments are equipped with a second fiber for simultaneous wavelength calibration. In the case of HARPS-N and CARMENES, we fed the second fiber with a Fabry-Pérot, while HARPS was fed by a simultaneous ThAr lamp.

In the case of HARPS and HARPS-N, the data were reduced by using the corresponding pipelines available at each observatory. In both cases, the pipeline also determines precise radial velocities using the cross-correlation function method (CCF, Baranne et al. 1996; Pepe et al. 2002) with a binary template of a similar spectral type as the target star. In the case of CARMENES, we use the CARACAL pipeline (Caballero et al. 2016) to perform the basic reduction, wavelength calibration and extraction of the spectra. Then, we used our own code *carmeneX*, partly based on the SERVAL pipeline (Zechmeister et al. 2018)², to compute the radial velocities by using the CCF technique with

² Publicly available at www.github.com/mzechmeister/serval.

Table 1. Summary of the data used in this paper for the nine targets analyzed, including the number of datapoints for each technique, both new (N_{new}) and from archive data (N_{arch}).

System	Radial Velocity				Lagrangian transit		TTV	
	N_{arch}	N_{new}	Inst. ^a	N_{tot}	N_{tr}	Inst.	N_{TTVs}	Ref.
GJ 3470	110	6/10	HN/C	126	1	CAFOS	25	[1]
HAT-P-12	23	6/5	HN/C	34	1	CAFOS	60	[2]
HAT-P-20	45	4/9/15	H/HN/C	73	3	CAFOS	33	[3]
HAT-P-23	36	0	-	36	3	CAFOS/WiFSIP	54	[4]
HAT-P-36	16	7/7	HN/C	30	3	CAFOS/WiFSIP	116	[5]
WASP-2	64	0	-	64	1	CAFOS	114	[6]
WASP-36	36	8/12/24	H/HN/C	80	2	CAFOS/WiFSIP	36	[7]
WASP-5	43	17	H	60	1	FORS2	33	[8]
WASP-77	16	7	C	23	4	CAFOS/WiFSIP	21	[9]

Notes. ^(a) Instruments are H = HARPS, HN = HARPS-N, C = CARMENES. [1] Awiphan et al. (2016), Bonfils et al. (2012), Poddaný et al. (2010) [2] Poddaný et al. (2010), Mallonn et al. (2015), Lee et al. (2012), Hartman et al. (2009) [3] Bakos et al. (2011), Bastürk et al. (2015), Poddaný et al. (2010), Granata et al. (2014), Sun et al. (2017) [4] Bakos et al. (2011), Poddaný et al. (2010) [5] Bakos et al. (2012), Poddaný et al. (2010) [6] Charbonneau et al. (2007), Collier Cameron et al. (2007), Hrudková et al. (2009), Southworth et al. (2010), Poddaný et al. (2010)] [7] Smith et al. (2012), Poddaný et al. (2010) [8] Hoyer et al. (2012) [9] Poddaný et al. (2010)

a solar-type binary mask with more than 3 000 spectral lines (adapted from the mask developed for CAFE, see Lillo-Box et al. 2015 and Aceituno et al. 2013).

We used HARPS in a five-night campaign³ on 21-25 January 2017 unfortunately affected by poor weather conditions, and only allowing us to use 1.5 nights due to high humidity, and in a monitoring campaign⁴ where we could gather 13 datapoints for WASP-5 over 4 months. In the case of HARPS-N, we had a three-night run⁵ on 6-8 February 2017 with successful observations during the whole campaign. Finally, we used CARMENES in a four-night run⁶ on 28-31 January 2017 with a success rate of 60%, mostly due to thick clouds and high humidity, and in another four-night run on 12-15 December 2017⁷ with a 48% success rate.

In Tables B.1 to B.7, we show the derived radial velocities and their uncertainties for the new radial velocity observations.

2.3. Differential photometry

We have used CAFOS (Meisenheimer 1994) at the 2.2 m telescope in Calar Alto Observatory, WiFSIP at the STELLA1 1.2 m robotic telescope (Strassmeier et al. 2010) of the Teide Observatory (Tenerife, Spain), and FORS2 (Appenzeller & Rupprecht 1992) at the Very Large Telescope (VLT, Paranal Observatory, ESO, Chile) to photometrically explore the regions around one of the Lagrangian points of the exoplanets studied in this work. The selection of the particular Lagrangian region (either L_4 or L_5) was done on the basis of previous radial velocity analysis in Lillo-Box et al. (2018a) for most of the targets. In Table B.8, we present the detailed characteristics of these observations for each of the targets. In all cases, the small eccentricities of the planets allow us to compute the transit times of the Lagrangian points as

$T_{0,\text{LP}} = T_0 \pm 1/6 \times P$, where T_0 is the planet mid-transit time, P is the orbital period, and the plus (minus) sign represents the L_5 (L_4) location. Based on this, we used the orbital properties from NASA Exoplanet Archive to compute the transit times by using the Transit Ephemeris Service⁸ at the corresponding location and custom phase. Since the radial velocity analysis is not sensitive to possible librations, the wider range of time we can observe around the Lagrangian point the better we will constrain the parameter space.

We used CAFOS (Calar Alto Faint Object Spectrograph) in imaging mode⁹ to obtain high-cadence relative photometry of eight of the targets. The field of view is reduced down to 7×7 arcmin (i.e., around 800×800 pixels for a plate scale of 0.53 arcsec/pix) to decrease the readout time and so increase the observational cadence. The exposure times for each target depend on their magnitudes and atmospheric conditions, ranging between 10-30 s in the SDSS *i* filter. The total time span for the observations is typically four hours centered on the Lagrangian point mid passage. We slightly defocused the telescope in order to increase the signal-to-noise ratio of the source, reaching an average of 50 000 counts per pixel. In the case of HAT-P-20, we defocused the telescope (both in CAFOS and WiFSIP observations) just up to 2 arcsec in order to avoid contamination from a close companion at 6.2 arcsec (Bakos et al. 2011). On the contrary, for WASP-77 we strongly defocused the telescope (up to donut-shaped point spread function) in order to merge the light from a close companion at 3 arcsec (Maxted et al. 2013) and so avoiding flux fluctuations inside the aperture due to possible seeing variations along the observation.

The CAFOS photometry was reduced with a custom aperture photometry pipeline¹⁰. The pipeline applies first the basic data reduction steps of bias subtraction and flat field division, after

³ Programme ID: ESO 098.C-0440(A), PI: J. Lillo-Box.

⁴ Programme ID: ESO 297.C-5051, PI: J. Lillo-Box.

⁵ Programme ID: 18-TNG4/16A, PI: D. Barrado.

⁶ Programme ID: CAHA F17-3.5-007, PI: Lillo-Box.

⁷ Programme ID: CAHA H17-3.5-024, PI: Lillo-Box.

⁸ <https://exoplanetarchive.ipac.caltech.edu/cgi-bin/TransitView/nph-visibletbls?dataset=transits>

⁹ Programme IDs: H17-2.2-018 and F18-2.2-004, PI: J. Lillo-Box

¹⁰ The pipeline is written in Python and built on top of Astropy (Astropy Collaboration et al. 2013), Photutils (Bradley et al. 2017), xarray (Hoyer

which it calculates the aperture photometry for the target star and a set of potential comparison stars using five aperture sizes. The final relative light curve is generated by finding a combination of comparison stars and aperture sizes that minimizes the relative light curve point-to-point scatter. A slightly modified version of the pipeline is used when the target star is accompanied by a bright nearby star (close enough for the PSFs to blend). In this case the photometry is calculated for a set of circular apertures and a set of elliptical apertures that contain the target and the contaminant. We calculate the relative target-contaminant flux based on the frames with best seeing, and remove the fractional contaminant flux from the combined flux (and use the circular aperture photometry centred on the target and contaminant to test that the contaminant is stable).

We also used WiFSIP (Wide Field STELLA Imaging Photometer) to explore the Lagrangian points of 3 exoplanets¹¹. The WiFSIP field of view is 22×22 arcmin and the plate scale corresponds to 0.322 arcsec/pix. In this case, given the robotic nature of the telescope and in order to increase the execution probability of the program, we asked observations of three times three hours around the Lagrangian point mid transit time, starting at random phases between two hours and half an hour before the start of the expected transit. The typical exposure times range between 10 and 80 s in the SDSSr band. In the same way as explained before, we also defocused the telescope for some targets (see Table B.8) in order to reach the maximum precision possible. The data have been reduced with the software tools used previously for high-precision exoplanet transit photometry with STELLA/WiFSIP (e.g., Mallonn et al. 2016). Bias and flat field correction was done with the standard STELLA pipeline. For aperture photometry we employed the publicly available tool SExtractor (Bertin & Arnouts 1996). Our software tools choose the selection of reference stars that minimize the standard deviation in the light curves, and by the same criterion also choose the best aperture size.

Finally, we also used FORS2 on 2016-10-26 in imaging mode with the z_SPECIAL filter to explore the L₅ region of WASP-5b during 3.68 hours¹². An individual exposure of 12 s was set, providing photon-noise limited images without need to defocus the telescope¹³. The FORS2 data was reduced and extracted following the same principles described above for the CAFOS data, using a similar (adapted) pipeline.

In all cases, regardless of the instrument used, the extraction procedure gathers a set of covariates (airmass, median sky level, full width at half maximum, and centroid shift of the target) that are used next to detrend the light curve (see § 3.2.1).

2.4. Transit timing variations

We have collected the transit times of all targets studied in this paper through the Exoplanet Transit Database (ETD, Poddaný et al. 2010). We only used transit epochs with data quality better or equal than 3, as flagged at the ETD. In the last two columns of Table 1, we show the number of epochs for each target together with the corresponding references.

et al. 2017), StatsModels (Seabold & Perktold 2010), NumPy (van der Walt et al. 2011), and SciPy

¹¹ Programme IDs: 52-Stella9/17B and 49-Stella4-18A, PI: D. Barrado

¹² Programme ID: ESO 298.C-5009, PI: J. Lillo-Box

¹³ Note that at the VLT, this can be done by doing bad-AO. However, this can introduce additional systematics in the relative photometry

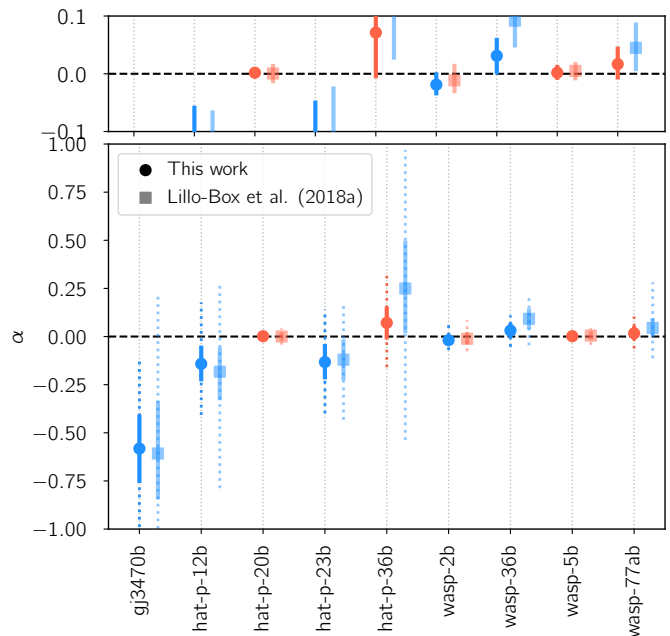


Fig. 1. Comparison between the α values obtained with the new data (circles) and the values published in Lillo-Box et al. (2018a). The colored dotted lines represent the 3σ uncertainties. Blue colors indicate $\alpha \pm \sigma > 0$ (i.e., candidate) and red colors indicate $\alpha - \sigma < 0 < \alpha + \sigma$ (i.e., no detection). The top panel is a close view of the region around $\alpha = 0$

3. Methodology: Constraining the parameter space

We use all the above described data to constrain the parameter space of a potential co-orbital planet. While the combination of the radial velocity and planet transit data (§ 3.1) can constrain the mass of the trojan (see Lillo-Box et al. 2018a; Leleu et al. 2017), the dedicated multi-epoch photometric exploration of the Lagrangian points (§ 3.2) and the measured transit timing variations of the planet (§ 3.3) can constrain other regions of the parameter space characterizing the co-orbital and its orbit. Here we explain each of these approaches.

3.1. Radial velocity + Planet transit

In all cases where new RV data from our own monitoring campaigns or from public data are available, we apply the same technique as in Lillo-Box et al. (2018a) based on the theoretical approach described in Leleu et al. (2017) to obtain an upper limit to the mass of the trojan and to decide on the Lagrangian point to be explored photometrically. This analysis is based on the determination of the α parameter which corresponds to $m_t/m_p \sin \zeta$ to first order in eccentricity, where m_t is the mass of the trojan, m_p is the mass of the planet, and ζ is the resonant angle representing the difference between the mean longitudes of the trojan and the planet. If α is significantly different from 0, the system is hence a strong candidate to harbor co-orbitals. Consequently, for a known planetary mass and an assumed resonant angle, an upper limit on α can be directly translated into an upper limit for the mass of trojans at the Lagrangian points. We will then obtain $m_{t,RV}^{\max}$ as the maximum mass (95% confidence level) that a potential trojan could have on the average location of the co-orbital along the observation timespan.

Table 2. Derived parameters for the nine planetary systems analyzed.

Object	V_{sys} (km/s)	P (days)	T_0 (BJD-2450000)	K (m/s)	α	c	d
gj3470b	$26.51640^{+0.00053}_{-0.00051}$	$3.33666^{+0.00011}_{-0.00010}$	$6090.47687^{+0.00047}_{-0.00044}$	$8.28^{+0.59}_{-0.60}$	$-0.58^{+0.16}_{-0.17}$	$-0.174^{+0.071}_{-0.074}$	$0.176^{+0.073}_{-0.072}$
hat-p-12b	$0.0002^{+0.0035}_{-0.0034}$	$3.2130599^{+0.0000063}_{-0.0000065}$	$4419.19555^{+0.00061}_{-0.00057}$	$38.6^{+1.9}_{-2.0}$	$-0.142^{+0.082}_{-0.080}$	$-0.062^{+0.039}_{-0.040}$	$-0.004^{+0.039}_{-0.036}$
hat-p-20b	$0.0874^{+0.0052}_{-0.0057}$	$2.8753186^{+0.0000053}_{-0.0000050}$	$6708.35627^{+0.00026}_{-0.00027}$	$1252.0^{+3.9}_{-4.2}$	$0.0018^{+0.0047}_{-0.0048}$	$-0.0140^{+0.0017}_{-0.0017}$	$0.0092^{+0.0035}_{-0.0034}$
hat-p-23b	$-0.007^{+0.017}_{-0.019}$	$1.212862^{+0.000042}_{-0.000039}$	$4852.26469^{+0.00055}_{-0.00054}$	359^{+15}_{-15}	$-0.132^{+0.082}_{-0.079}$	$-0.001^{+0.018}_{-0.017}$	$-0.098^{+0.034}_{-0.039}$
hat-p-36b	$0.007^{+0.032}_{-0.028}$	$1.3273435^{+0.0000074}_{-0.0000071}$	$5565.18152^{+0.00053}_{-0.00057}$	$327^{+8.1}_{-10}$	$0.071^{+0.072}_{-0.075}$	$0.020^{+0.024}_{-0.020}$	$-0.037^{+0.022}_{-0.023}$
wasp-2b	$-27.864^{+0.011}_{-0.011}$	$2.1522215^{+0.0000012}_{-0.0000013}$	$3991.51537^{+0.00048}_{-0.00053}$	$152.9^{+3.7}_{-3.5}$	$-0.019^{+0.018}_{-0.015}$	$-0.0016^{+0.0036}_{-0.0035}$	$0.027^{+0.024}_{-0.027}$
wasp-36b	$-13.211^{+0.011}_{-0.010}$	$1.5373595^{+0.0000044}_{-0.0000043}$	$5569.83733^{+0.00028}_{-0.00027}$	$375.8^{+2.8}_{-2.8}$	$0.031^{+0.027}_{-0.029}$	$-0.0029^{+0.0094}_{-0.0088}$	$0.0290^{+0.0090}_{-0.0090}$
wasp-5b	$20.0174^{+0.0075}_{-0.0079}$	$1.6284261^{+0.0000020}_{-0.0000021}$	$4375.62495^{+0.00073}_{-0.00075}$	$267.4^{+1.3}_{-1.4}$	$0.0019^{+0.0096}_{-0.0088}$	$-0.0036^{+0.0026}_{-0.0027}$	$-0.0020^{+0.0055}_{-0.0062}$
wasp-77ab	$1.6604^{+0.0086}_{-0.0081}$	$1.3600332^{+0.0000048}_{-0.0000049}$	$5870.44975^{+0.00043}_{-0.00043}$	$325.3^{+6.7}_{-6.4}$	$0.017^{+0.027}_{-0.023}$	$0.00165^{+0.00099}_{-0.00095}$	$0.047^{+0.031}_{-0.030}$

We followed the same procedure as in our previous work, modeling the radial velocity with the equation described in Leleu et al. (2017) and including a Gaussian Process to account for the presence of active regions in the stellar surface that can lead to correlated noise in the data. To this end we used a quasi-periodic kernel (described in Faria et al. 2016). We set Gaussian priors for the orbital period, time of mid-transit of the planet, and $c \approx e \cos \omega$ when this parameter can be constrained from the detection of the secondary eclipse. These priors are centered on the values from the literature and we set a width equal to three times the estimated uncertainties provided in the literature. Log-uniform priors are set to the GP hyperparameters and uniform priors are used for the rest of the parameters, including the systemic velocity (V_{sys}), the radial velocity semi-amplitude (K), α , and $d \approx e \sin \omega$. The results of the RV fitting are shown in Fig. A.1 and the median and 68.7% confidence values of the main fitted parameters are shown in Table. 2, and will be discussed individually in § 4. Also, in Fig. 1, we compare the α values for these nine systems between the current work and our first analysis in Lillo-Box et al. (2018a). The main conclusion is that we can reduce the uncertainty in systems where a significant amount of new data points were obtained compared to the previous data. This allows to set lower upper mass limits. For instance, in the case of HAT-P-36 and WASP-77A, the α parameter is now compatible with null within 1σ .

3.2. Photometric exploration of the Lagrangian points

The photometric exploration of the Lagrangian points can constrain: i) the trojan size, if we assume small librations around the Lagrangian point; and ii) the orbital parameters of the co-orbital body, specially the libration amplitude assuming coplanarity. In the following section we describe the different analysis of the precise photometry obtained during our ground-based campaigns. Each subsection focuses on particular aspects, namely individual transit searches on each epoch assuming coplanarity and hence similar transit duration as the planet (§ 3.2.1), the implications of non detection on the trojan libration amplitude (§ 3.2.2), and transit search on the combined light curve assuming no libration (§ 3.2.3).

3.2.1. Individual epochs (coplanar case): search for transits

We used the different epochs for a single system independently to look for transits in the observed timespans. The search is done through transit fitting of the light curve, which also allows us to estimate the maximum object size in case no transit is detected. This fit is done by using the *batman*¹⁴ python module (Kreidberg 2015), where we assume a Gaussian prior on the orbital period (P), semi-major-axis to stellar radius (a/R_{\star}) and inclination (i) parameters. This implies that we are looking for coplanar (or very close to coplanar) trojans, thus having transit durations similar to that of the planet. But, we note that not completely fixing these values still allows for some freedom in the trojan transit duration. We then leave the mid-transit time of the trojan ($T_{0,t}$), the trojan-to-stellar radius (R_t/R_{\star}), the zero level (out-of-transit flux level, F_0), and a photometric jitter to account for white noise (σ_{jit}), as free parameters with uniform priors. The specific priors and ranges are shown in Table 3. We also include a baseline model simultaneously to account for possible correlations with airmass (χ), seeing (s , full width at half maximum of the target point spread function), time (t), position of the target on the detector (xy) and background (b). In a first stage, we use linear dependencies for these parameters, $\mathcal{B}(t, \chi, s, x, y, b)$. Mathematically, the baseline model can be represented as $\mathcal{B} = \sum_i a_i p_i$, where a_i are the coefficients to be determined and p_i are each of the parameters described above. The baseline and transit models are fitted simultaneously, assuming that each datapoint is a realization of $d(t) = \mathcal{B}(p) + \mathcal{T}(t) + \sigma_{\text{jit}}$.

We use *emcee*¹⁵ (Foreman-Mackey et al. 2013) with 50 walkers and 50 000 steps per walker to explore the posterior distribution of the transit parameters and baseline coefficients. We use the last half of each chain to compute the final posterior distributions and parameter-parameter dependencies. We test a model with trojan (trojan-hypothesis) and without trojan (null-hypothesis). In the latter case the number of free parameters reduces to F_0 , σ_{jit} and the baseline parameters. The bayesian evidence (E) of these two models are estimated using the *perrakis*

¹⁴ <http://astro.uchicago.edu/~kreidberg/batman/>

¹⁵ See <http://dan.iel.fm/emcee> for further documentation.

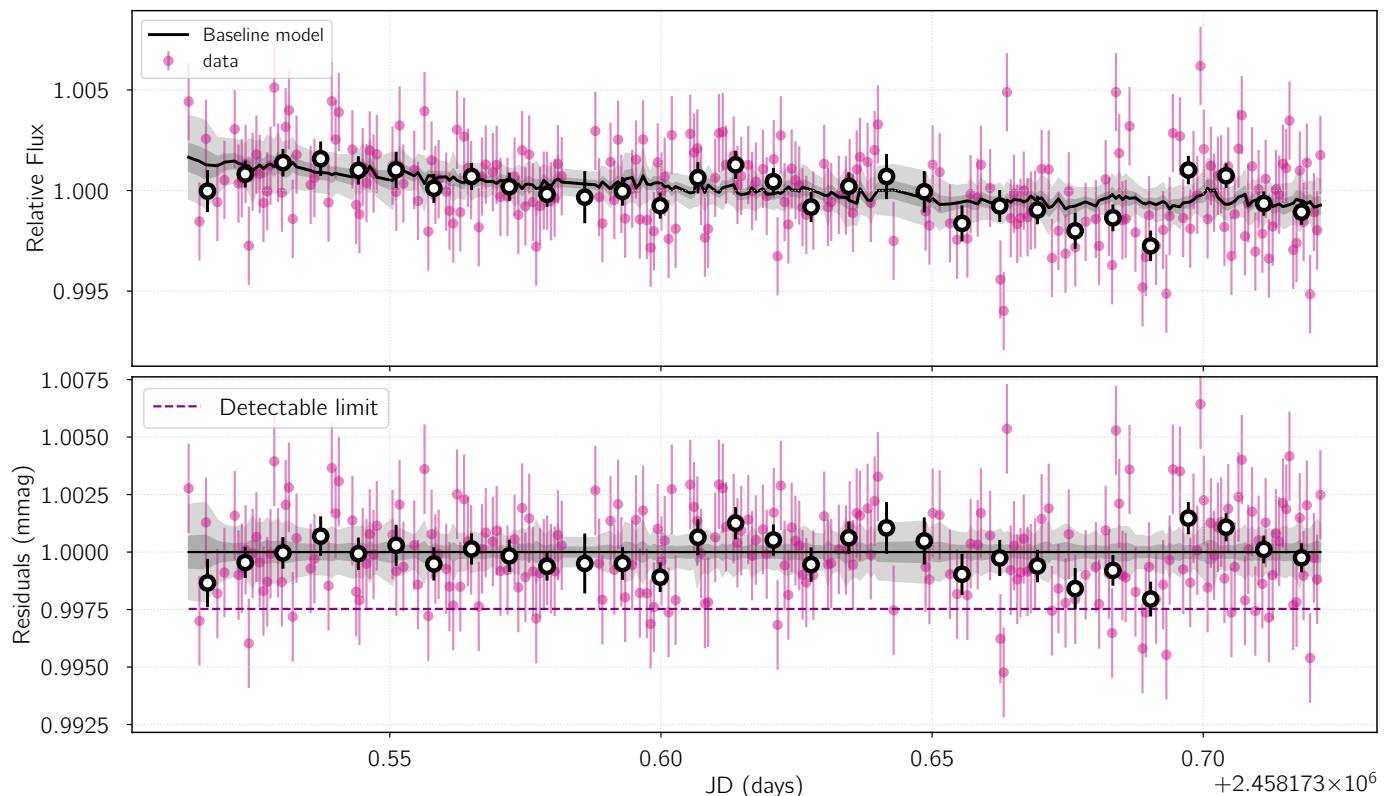


Fig. 2. Example of the light curve analysis of the L₅ region of HAT-P-36 b (observed with CAFOS on 2018-03-22) including the linear baseline model (see Sect. 3.2.1). The upper panel shows the raw light curve (violet symbols) together with the 15-min binned data (black open circles, for visualization purposes) and the baseline model fitted. In this case, we assume to trojan (null hypothesis). The bottom panel shows the baseline-corrected light curve with the detectable limit calculated as the 95% interval for the R_t/R_\star parameter in the trojan model. In both panels, the shaded regions correspond to the 68.7% and 99.7% confidence intervals.

Table 3. Priors for the light curve analysis and transit fitting.

Parameter	Prior	Units
$\dagger T_{0,t}$	$\mathcal{U}\left(\min(t) - \frac{T_{\text{dur}}}{4}, \max(t) + \frac{T_{\text{dur}}}{4}\right)$	days
$\dagger P_{\text{orb}}$	$\mathcal{G}(\mu, \sigma)$	days
$\dagger a/R_\star$	$\mathcal{G}(\mu, \sigma)$	-
$\dagger R_t/R_\star$	$\mathcal{U}(0, R_p)$	-
$\dagger i$	$\mathcal{G}(\mu, 3\sigma)$	degrees
F_0	$\mathcal{U}(-0.3, 0.3)$	-
σ_{jit}	$\mathcal{U}(0, 5)$	mmag

Notes. ^(†) These parameters are only included in the models with trojan (i.e., not in the null-hypothesis tests). $\mathcal{U}(a, b)$ stands for uniform priors between a and b , while $\mathcal{G}(\mu, \sigma)$ represents a Gaussian prior with mean μ and standard deviation σ .

code¹⁶. Based on this Bayesian evidence, we can estimate the Bayes factor (BF) between the two models as the ratio between the evidence of the trojan hypothesis (E_t) and the null hypothesis (E_0), so that $BF = \ln E_t - \ln E_0$. A positive BF would favor the trojan hypothesis against the null hypothesis, with $BF > 6$ considered as a strong evidence.

¹⁶ <https://github.com/exord/bayev>. This code is a *python* implementation by R. Díaz of the formalism explained in Perrakis et al. (2014).

Additionally, the posterior distribution of the trojan-to-star radius ratio (R_t/R_\star) is checked. If this parameter is significantly different from zero (i.e., the median value is larger than the 95% confidence interval) and the Bayes factor favors the trojan-hypothesis against the null-hypothesis, then we consider that we have a candidate trojan transit. In this case, we proceed by testing models (both with and without trojan) with quadratic dependencies for the baseline parameters, $p(t^2) + p(\chi^2) + p(s^2) + p(xy^2) + p(b^2)$. More specifically, we first run all parameters with quadratic dependencies, then we check the relevant parameters producing significant non-zero coefficients in the fit and we finally run a last model only including those relevant parameters. We then re-estimate the Bayesian evidence and look for the model with the largest evidence. If that model corresponds to a trojan-hypothesis model and keeps the significance of the R_t/R_\star parameter, then we consider the transit as a strong trojan transit candidate.

In the cases where no significant transit was detected, we can determine a maximum radius of the trojan per each epoch (R_{t,TR_i}^{max}). This is determined as the 95% confidence interval of the posterior distribution of the R_t/R_\star parameter. We also establish a time interval (which can be translated to a phase interval) where we can assure that there is no transit of a body larger than R_{t,TR_i}^{max} . This time interval is considered as the entire observing window, which implies that we only consider a transit detection if we have more than half of the transit. We note that this is a conservative assumption for constraining the parameter space. An example of this approach is shown in Fig. 2 for the transit of the L₅ Lagrangian point of HAT-P-36 b observed with CAFOS. The figure

shows the modeling with the null hypothesis and the detectable limit by this observations in the bottom panel (dashed horizontal line). In Fig. A.2-A.4 we show for all nine systems the results of the null-hypothesis models once the fitted baseline contribution has been removed.

3.2.2. Individual epochs (coplanar case): parameter space constraint

We can then use the time range of non-detected transit for each epoch to constrain the parameter space of the trojan orbit. We can do this by determining the parameter range where the trojan would not transit during these time ranges (assuming the trojan is larger than the above estimated maximum radius). To this end, we apply a Monte-Carlo Markov-Chain (MCMC) using a modified likelihood function (\mathcal{L}) which increases towards the edges of the observed time ranges and is flat and maximum outside of them:

$$\mathcal{L}_i = -0.5 \ln 2\pi + \ln(\sigma^2) + \frac{r^2}{\sigma^2} \quad (1)$$

where

$$r = \begin{cases} \phi_{\text{mid}} - x & \text{if } (\phi_{\text{in}} < x < \phi_{\text{out}}) \ \& \ (R_t > R_t^{\text{max},i}) \\ \phi_{\text{mid}} - \phi_{\text{in}} \equiv \mathcal{L}_i^{\text{max}} & \text{if } (\phi_{\text{in}} < x < \phi_{\text{out}}) \ \& \ (R_t < R_t^{\text{max},i}) \\ \phi_{\text{mid}} - \phi_{\text{in}} \equiv \mathcal{L}_i^{\text{max}} & \text{if } x < \phi_{\text{in}} \ \text{or} \ x > \phi_{\text{out}} \end{cases} \quad (2)$$

where ϕ_{in} and ϕ_{out} are the orbital phases corresponding to the earliest and latest edge of the time range (i.e., t_{in} and t_{out}). ϕ_{mid} represents the mid time of this time range and σ is one fourth of this time span. Consequently, the likelihood is minimum at the mid time of the observations and is maximum and constant outside of this range. The total likelihood (\mathcal{L}) is the sum of the likelihoods ($\sum_i \mathcal{L}_i$) calculated as above for each transit epoch observed.

The model calculates the expected time (or orbital phase) of the mid-transit based on the projected position of the trojan in the sky, which can be simplified from Eqs. 53-55 in Murray & Correia (2010) for small eccentricities as

$$\begin{aligned} X_t &= a/R_\star \left[\cos \lambda_t + e_t/2 \left(-3 \cos \omega_t + \cos(2\lambda_t - \omega_t) \right) \right] \\ Y_t &= a/R_\star \left[\sin \lambda_t + e_t/2 \left(-3 \sin \omega_t + \sin(2\lambda_t - \omega_t) \right) \right] \cos i \\ Z_t &= a/R_\star \left[\sin \lambda_t + e_t/2 \left(-3 \sin \omega_t + \sin(2\lambda_t - \omega_t) \right) \right] \sin i, \end{aligned} \quad (3)$$

where e_t and ω_t are the trojan eccentricity and argument of the periastron; λ_t is the mean longitude of the trojan; i is the orbital inclination; and a/R_\star is the semi-major axis to stellar radius ratio. Based on these equations and the reference frame described in Leleu et al. (2017), the trojan transit occurs when $X_t = 0$ (conjunction), $|Y_t| < 1$ (the object does transit the star), and $Z_t < 0$ (primary eclipse). Hence, we can calculate the times at which these conditions are fulfilled (i.e., the mid-times of the trojan transit on each orbit) and, in particular, at the orbits that we observed.

By comparing these values with the time ranges for each epoch we can constrain the parameter space of the parameters involved so that transits do not occur during these time ranges. To that end, we use 20 walkers with 50 000 steps per walker in our MCMC and we only select the steps with \mathcal{L} equal to the sum of the maximum likelihoods on each epoch, i.e., $\sum_i \mathcal{L}_i^{\text{max}}$. With these selected steps (usually around 80% of the original chain) we can then construct the corner plot diagram with

the parameter-parameter dependencies of the orbital models not having trojan transits during the observed time ranges. This diagram provides the constraints of the parameter values based on the observed photometric data in the absence of trojan transits and can be used, for instance, to provide a minimum libration amplitude for the trojan. In case several epochs were observed, we include the possibility of an eccentric orbit for the trojan. In case only one epoch is available, we assume circular orbit for the trojan ($e_t = 0$).

As a matter of example, we show in Fig. 3 the results for the analysis of WASP-77A. The red vertical lines represent the orbital phase interval that we observed, finding no transits. The expected transit is marked by the horizontal lines (dotted line being the expected ingress and egress phases). The colored lines represent a sample of accepted models from the whole MCMC chain. For a model to be accepted it has to either not cross the red lines if the trial trojan radius is larger than the light curve detectability limit (blue colored lines), or if the trojan transits during our observations but it is smaller than the detectability limit (green lines). In this particular example, our data allows us to reject trojans larger than $4 R_\oplus$ with librations amplitudes shorter than 25° .

3.2.3. Combined epochs

Finally, we can also combine all epochs for the same object and Lagrangian point by assuming that the would-be transits are achromatic, given that we observed with different filters on different telescopes. This provides a smaller maximum radius of the trojan in case of no libration or in the case that the libration period is much larger than the time span of the observations. To do this we remove the median baseline model for each epoch in the null hypothesis and then combine all epochs in orbital phase (see Fig. 4). We now try to search for a transit in this combined lightcurve in order to get a maximum radius for a stationary trojan (i.e., with no libration). To this end we follow the same procedure as in § 3.2.1.

We can translate the maximum trojan radius into a maximum trojan mass by using the *forecaster* module (Chen & Kipping 2017). According to the documentation of this module, it provides accurate estimates of the masses in the case of terrestrial and Neptune-like worlds, which are the typical cases for the radius limits found in this paper.

3.3. Transit timing variations

As presented in Ford & Holman (2007), the amplitude of the variations in the transit times of the hosting planet (K_{tt}) due to the libration of a trojan with amplitude¹⁷ K_ζ are well represented by the Eq.1 in that paper, i.e.,

$$K_{tt} = 60 \text{ s} \left(\frac{P_{\text{orb}}}{4 \text{ days}} \right) \left(\frac{m_t}{m_\oplus} \right) \left(\frac{0.5 M_{\text{Jup}}}{m_p + m_t} \right) \left(\frac{K_\zeta}{10^\circ} \right). \quad (4)$$

If no periodic variations are found, we can estimate an upper limit for this amplitude by simply fitting a sinusoidal function to the measured TTVs, with amplitude K_{tt} . This way, we can find a direct relation between the trojan mass and the libration amplitude, thus constraining this parameter space. We can compute the maximum TTV amplitude ($K_{tt,\text{max}}$) as the 95% confidence

¹⁷ Note that $\zeta = \lambda_p - \lambda_t$ is the angular difference between the mean longitude of the planet (λ_p) and the mean longitude of the trojan (λ_t).

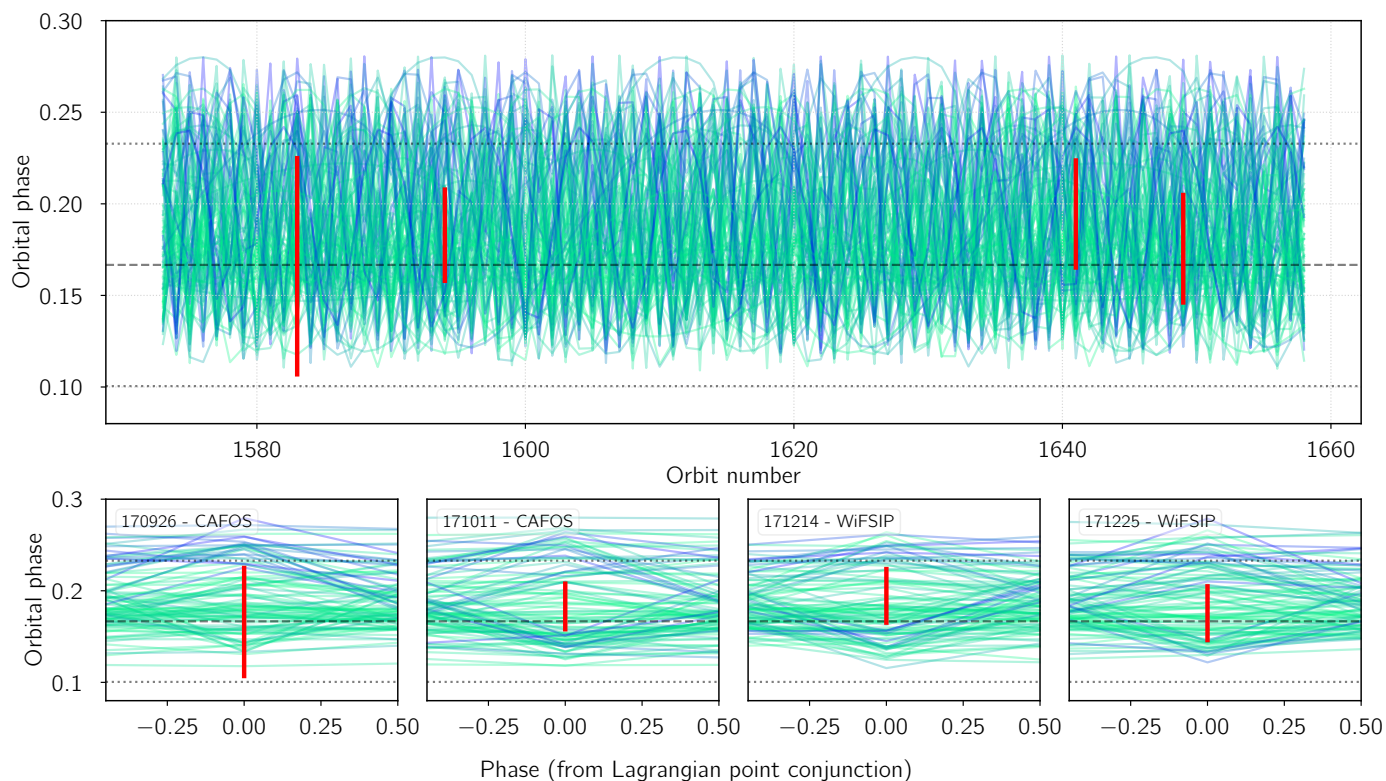


Fig. 3. Example of the analysis of the parameter space constrain based on the non-detection of transits in our data for the system WASP-77A. The upper panel shows the orbit number (X-axis) versus the orbital phase covered by our observations (red vertical lines). The transit of the Lagrangian point (L_5 in this case) is expected to happen between the dotted horizontal lines. The colored lines represent a small sample of the accepted models. For a model to be accepted it has to either not cross the red lines if the trial trojan radius is larger than the light curve detectability limit (blue lines) or if the trojan transits during our observations but it is smaller than the detectability limit (green lines). The bottom panels are just close views on each of the four epochs, with the X-axis being the phase from the Lagrangian point conjunction.

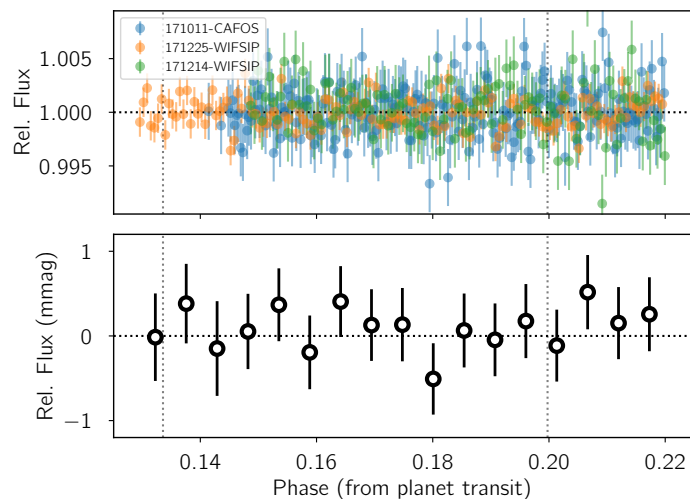


Fig. 4. Example of the light curve combination in phase for the case of WASP-77A. The individual epochs are shown in the upper panel (after removing the linear baseline model) and the combined light curve is shown in the bottom panel with 10-min bins having 225 ppm rms. The vertical dotted lines mark the expected transit ingress and egress of the Lagrangian point.

level from the marginalized posterior probability of K_{tt} . In tadpole low eccentricity orbits, we expect the libration of the trojan to introduce sinusoid-like variations in the planet’s time of transit. Hence, under this assumption, we can use the simple model

$Z + K_{tt} \sin(\nu_{lib}t + \phi_{tt})$, being ν_{lib} the libration frequency (Leleu et al. 2015), ϕ_{tt} a phase offset, and Z a zero level to account for the uncertainties in the orbital period and mean mid-transit time. We assume a uniform prior for all parameters involved in the model, with $Z \in \mathcal{U}(-0.1, 0.1)$ hours, $K_{tt} \in \mathcal{U}(0.0, 5.0)$ hours, $\nu_{lib} \in \mathcal{U}(\nu_{LP}/5, 5\nu_{LP})$ with $\nu_{LP} = 2\pi/P_{orb} \sqrt{27/4 m_p/(m_p + M_\star)}$, and $\phi_{tt} \in \mathcal{U}(0, 2\pi)$.

In order to sample the posterior distribution we use an MCMC algorithm by means of the *emcee* code. We use 50 walkers and 100 000 steps per walker. We remove the first half of the steps and compute the marginalized posterior distribution for the K_{tt} parameter. We check that the posterior distribution is actually truncated at $K_{tt} = 0$ (i.e., no detection of periodic TTVs). Then, the 95% percentile is computed to obtain $K_{tt,max}$. Given this value, we can get a contour in the $m_t(K_{tt})$ function to constrain the parameter space.

3.4. Constraints to the trojan mass vs. libration amplitude parameter space

The analysis described above for the the multi-technique data produces different constraints on several planes of the parameter space. One interesting plane is the trojan mass versus the libration amplitude, because it provides both physical and dynamical information relevant for detection purposes. In Fig. 5, we show an example of the constraints provided by our analysis on this plane assuming coplanarity between the trojan and planet orbital planes. The analysis of the radial velocity provided in § 3.1 constrains the mass of the trojan regardless of the libra-

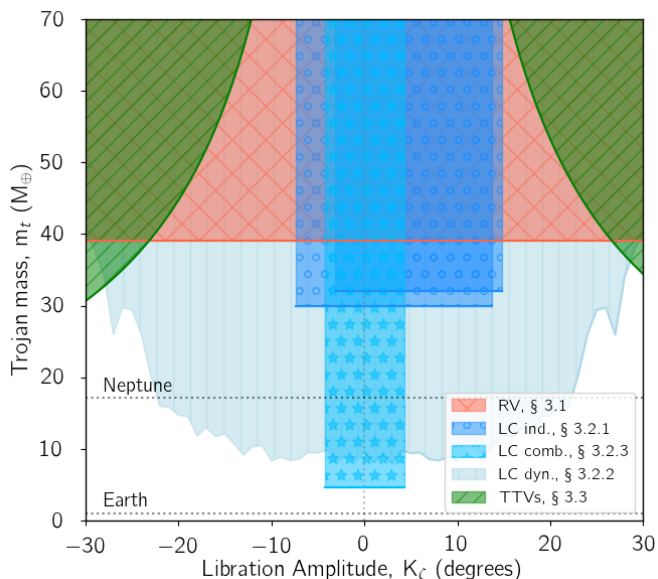


Fig. 5. Detailed example of the constraining of the trojan mass versus libration amplitude parameter space in the case of WASP-77A. Negative (positive) values for the libration amplitude are used to represent constraints on transits before (after) the Lagrangian point passage. Only the white region is not explored by our data.

tion amplitude, since the data was taken during a long timespan (much longer than the libration period). This is shown by the red shaded region in the example Fig. 5. In order to translate the results from the light curve analysis (from the individual analysis - § 3.2.1-, the dynamical analysis combining the individual epochs - § 3.2.2-, and from the combined light curve - § 3.2.3), we convert the maximum trojan radius to maximum trojan masses by using the *forecaster* module (Chen & Kipping 2017). The libration parameter in this case is constrained by the time range of our observations in the case of individual light curves and from the expected transit duration for the combined light curves. Finally, the TTVs can constrain this parameter space as already described in § 3.3 (shown in green in the example Fig. 5). The diagram corresponding to each of the nine systems can be found in Fig. A.5.

4. Results per system

Based on the analysis of the multi-technique data presented in section 3, we can now constrain the presence of co-orbital bodies in the surroundings of the Lagrangian points in these nine systems. Here we summarize the results for each of the analyzed planetary systems.

4.1. GJ 3470

Only one Lagrangian transit is available for this system. The analysis of the light curve shows no significant detection of any transit up to $3.7 R_{\oplus}$. The analysis of the radial velocity data provides a value for the α parameter significantly different from zero. However, the eccentricity fitted is too large and thus the radial velocity equations are out of the validity range (i.e., $e < 0.1$). Consequently, the result is degenerate and we can neither discard the trojan scenario nor confirm it. In order to solve this dichotomy, a measurement of the secondary eclipse of the planet

would be needed¹⁸, together with the development of new equations with a wider eccentricity validity range. Also, the TTVs do not show a significant periodic variation up to 3.2 minutes. This allows us to put important constraints on the mass of any potential librating trojan and confirms that should it exist with a moon- or planet-size, the libration amplitude should be smaller than 4° for trojans with masses larger than Earth and smaller than 10° for sub-Earth-mass trojans.

4.2. HAT-P-12

The photometric exploration of L_4 in HAT-P-12 did not show any significant dim down to $4.8 R_{\oplus}$. However, only half of the Lagrangian point passage could be covered with CAFOS due to bad weather conditions. The radial velocity analysis provides $\alpha = -0.141 \pm 0.082$, corresponding to a trojan mass of $10.8 \pm 6.3 M_{\oplus}$ at L_4 . This sets an upper limit of $21 M_{\oplus}$ in L_4 and rejects any trojan more massive than $4 M_{\text{Moon}}$ at L_5 . The TTVs in this system restrict the libration amplitude importantly, leaving only sub-Earth masses to libration amplitudes larger than $\sim 7^{\circ}$. Hence, if larger bodies are present in this Lagrangian point, low libration amplitudes are expected and so sub-mmag precision light curves could explore this regime (an Earth-size body would induce ~ 170 ppm transit depth in this system). This system illustrates that since TTVs are proportional to the trojan-to-planet mass, small co-orbitals should be more easily found co-rotating with low mass planets.

4.3. HAT-P-20

The large amount of radial velocity data that we gathered for HAT-P-20 b added to the archive spectra allows now to estimate $\alpha = 0.0017 \pm 0.0048$. This very small value allows us to set an upper limit on the mass of any potential trojan of $25 M_{\oplus}$. The TTVs do not show any clear periodic sinusoidal signal. However, the data show variations up to 2.5 minutes peak-to-peak.

A total of three observations of the L_5 transit passage have been observed with CAFOS for this target. The quality of the observations is very variable, going from very bad quality (on 2017-04-03 with flux variations up to 5 mmag) to very good quality data at the ~ 1.5 mmag level on individual measurements. We have tested the null hypothesis and the trojan hypothesis in all three epochs. The results show that for two epochs (2017-04-03 and 2017-11-16) the null hypothesis has a significantly larger evidence than the trojan hypothesis. They both allow us to set upper limits on the trojan size of $8.3 R_{\oplus}$ and $2.9 R_{\oplus}$ (respectively) in the phases covered by these epochs.

However, the results on the night of 2017-12-09 provide a larger evidence to the trojan model against the null hypothesis, showing a Bayes factor of 12 in favor of the trojan model. These two models (with and without trojan) are built on the basis of linear dependencies with the baseline parameters. We have also tested different quadratic dependencies for the null hypothesis but all of them show Bayes factors even larger in favor of the trojan linear-baseline model. This favored model reveals a dim in the light curve at phase 0.195 that would correspond to a $5.8 R_{\oplus}$ object. In Fig. 6, we show the CAFOS light curve with the baseline model removed and the median fitted transit model. Despite the large significance of the trojan model, the large radius of the possible co-orbital is puzzling (although it could also be

¹⁸ The estimated eclipse depth for this planet is smaller than 25 ppm. This is at the limit precision that will be achievable by the *James Webb Space Telescope*.

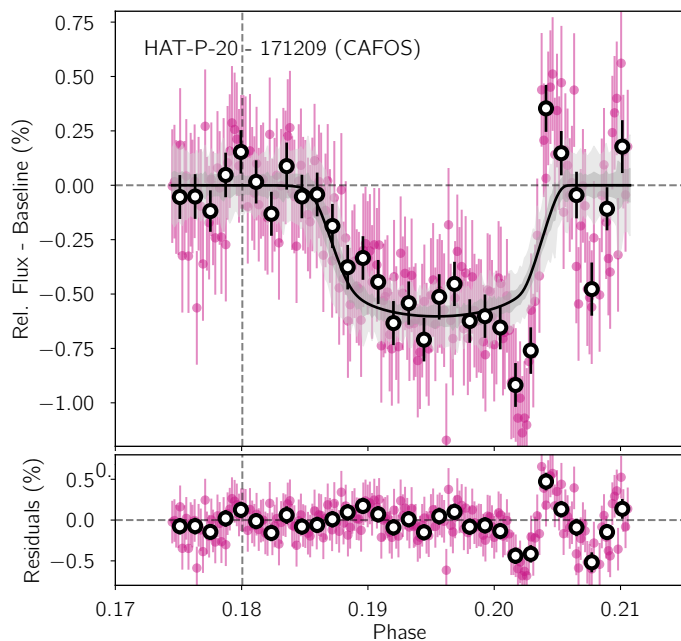


Fig. 6. Trojan hypothesis model after removing the linear baseline model for HAT-P-20. This trojan model is only favored against the null hypothesis if we include the whole data set. However by removing the feature at phases $\phi > 0.20$, the null hypothesis is favored. The black shaded vertical line represents the expected egress of the Lagrangian point, showing the large time lag of the would-be trojan transit. This light curve corresponds to the data from CAFOS at CAHA on 2017-12-09.

a compact trojan swarm). Also, the baseline models without trojan are able to reproduce qualitatively well the would-be ingress, removing the transit signal. In Fig. A.2 (in the panel labeled as "HAT-P-20 - 171209"), this non trojan model is shown.

As easily pointed out in both figures, at phases larger than 0.20 there is a clear modulation that any baseline model fails to reproduce. In order to test if this might be the only reason why the trojan model is favored against the non-trojan model we performed the same analysis by removing all datapoint after phase $\phi > 0.20$ (after Julian date 2458097.2121). The results of this analysis, however, increase the significance of the non-trojan model providing an evidence 12 times larger now in favor of the null hypothesis. We then conclude that the strong modulation at the end of our observations strongly affects the result of the analysis and so we cannot conclude on the presence of any large body in this transit with the current data. Since this deep event (that would correspond to a gas giant) is not seen neither in the other epochs nor in the radial velocity data, we assume for the subsequent discussion that no trojan is present in this system.

Under this assumption, the analysis of the combined light curve produces an upper limit on the trojan mass of $2 R_{\oplus}$ at the exact Lagrangian point.

4.4. HAT-P-23

In the case of HAT-P-23, we found $\alpha = -0.132 \pm 0.082$, corresponding to a 95% upper limit of $205 M_{\oplus}$. We photometrically explored the L_4 region during three different passages of this region in front of its star. We can discard coplanar transits in these observations of objects up to $5.1 - 6.2 R_{\oplus}$. Furthermore, the combined light curve allows discarding bodies larger than $1.39 R_{\oplus}$ laying exactly at the Lagrangian point (or experienc-

ing very small librations). The analysis of the parameter space of the trojan properties that still remain plausible despite of the non transit detection, just leaves the possibility of large libration amplitudes for circular orbits of the trojan, which are avoided by the lack of TTV modulations. Hence, should it exist, the trojan co-orbiting to HAT-P-23 b must be either a planet smaller than Neptune with a large libration amplitude or a low mass ($< 4 M_{\oplus}$) planet in a low libration amplitude but highly-eccentric orbit.

4.5. HAT-P-36

Photometric variability at the 1.5 mmag level appears in the CAFOS and WiFSIP light curves around the L_5 region, which might be due to the moderate activity of the host star ($\log R' = -4.65$ dex, Mancini et al. 2016). No significant dim is detected down to $6 R_{\oplus}$ at L_5 in the CAFOS light curve (the WiFSIP data being of slightly worse quality in this case). The new radial velocity measurements presented in this paper allow us now to decrease the α parameter to $\alpha = 0.071^{+0.072}_{-0.076}$ (from the previous $0.25^{+0.22}_{-0.24}$), thus being now fully compatible with no trojan at $1-\sigma$ level. This now corresponds to a maximum mass of the trojan of $128 M_{\oplus}$ at L_5 (around four times smaller than our previous upper limit) and $38 M_{\oplus}$ at L_4 . However, the combination of all three available transit observations allows us to set small upper radius of $2 R_{\oplus}$ to any trojan body located at the exact Lagrangian point.

4.6. WASP-2

In this case we find $\alpha = -0.018^{+0.018}_{-0.015}$, so that we can set an upper limit to the trojan mass of $15.1 M_{\oplus}$, similar to our previous measurement. The analysis of the TTVs also do not show any significant periodic variation and the single transit we could observe with CAFOS do not show any significant dim. The upper limit that we can impose based on this non-detection of the transit is $4.3 R_{\oplus}$. The TTVs also indicate that trojans more massive than the Earth should have libration amplitudes smaller than 25° .

4.7. WASP-36

The 14 new radial velocity measurements obtained for this target with HARPS-N and CARMENES allows us to decrease the significance in the α parameter with respect to Lillo-Box et al. (2018a). We find now $\alpha = 0.031 \pm 0.028$ (compared to the previous 0.092 ± 0.043). We have now decreased by two the uncertainty in this parameter. However, due to the large mass of the planet, we can only set an upper limit to its trojan mass at L_5 of $m_t < 63 M_{\oplus}$ (compared to the previous $146 M_{\oplus}$). Additionally, the TTVs do not show variations larger than 320 s. Finally, the two WiFSIP observation of the Lagrangian transit do not show any dim down to $8 R_{\oplus}$ and $5.4 R_{\oplus}$, respectively. The combined lightcurve, however, provides a much smaller upper limit to the size of any potential trojan of $2.1 R_{\oplus}$. This allows us to reject any possible trojan with $m_t > 10 M_{\oplus}$ at the exact position of the Lagrangian point.

4.8. WASP-5

The new radial velocity analysis presented in this work (including new HARPS data) now provides $\alpha = 0.002 \pm 0.010$, corresponding to an upper limit of $10.4 M_{\oplus}$ at L_5 and $7.6 M_{\oplus}$ at L_4 . The periodogram of the TTVs in this case shows a peak around 18 days although this peak is not statistically significant. The

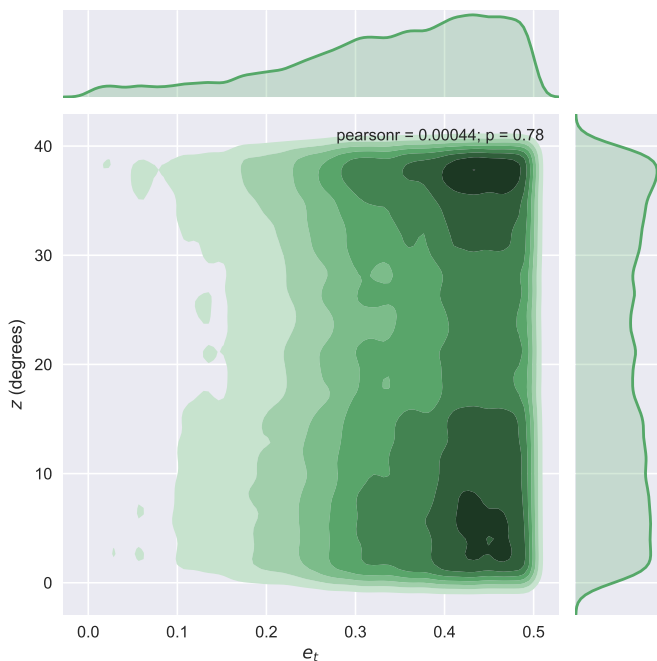


Fig. 7. Parameter space of trojan’s eccentricity versus libration amplitude constrained by the non-detection of transits in the four Lagrangian passages observed for WASP-77A b. The results show that only highly eccentric orbits are possible for any libration amplitude and that low eccentric orbits are still allowed for libration amplitudes larger than 35° .

modeling of the TTVs consistently provides a possible periodic solution with an amplitude of $K_{tt} = 32 \pm 18$ s and a periodicity of $P_{tt} = 18.06^{+0.17}_{-0.96}$ days. If we neglect the mass of the trojan, the expected libration period would be 15.7 days in this system. But, this periodicity can be elongated due to different factors like mutual inclination or eccentricity.

Using Eq. 1 in Ford & Holman (2007) we can use the estimated K_{tt} to get a relation between the trojan mass and the libration amplitude. Given the upper limit on the mass provided by the radial velocity analysis, and assuming the TTV modulations, the possible trojan should have a minimum libration amplitude of 4° . The lower the trojan mass the larger libration amplitude is needed to produce the observed TTV modulation.

Such low libration amplitude implies that the trojan could transit the star very close to the Lagrangian point passage on every orbit. The upper mass limit of $10.4 M_\oplus$ provided by the radial velocity would correspond to an object of $3.1^{+1.4}_{-0.8} R_\oplus$. Our FORS2 observations of the L_5 passage do not show any statistically significant dim, providing an upper limit on the trojan radius of $4.5 R_\oplus$. Hence, we would need at least two more transits to test the regime allowed by the radial velocity.

4.9. WASP-77

The new RV data from CARMENES allows us now to decrease the upper limit in the mass of any potential trojan by a factor of four, now being $\alpha = 0.017 \pm 0.027$, corresponding to an upper mass limit of $39 M_\oplus$ (compared to the $92 M_\oplus$ obtained in our previous analysis, Lillo-Box et al. 2018a). The photometric data from the four epochs do not show statistically significant dims. Having four epochs allows us to set important constraints on the orbital properties of any potential trojan detectable with our photometric data but not transiting during our observing time ranges

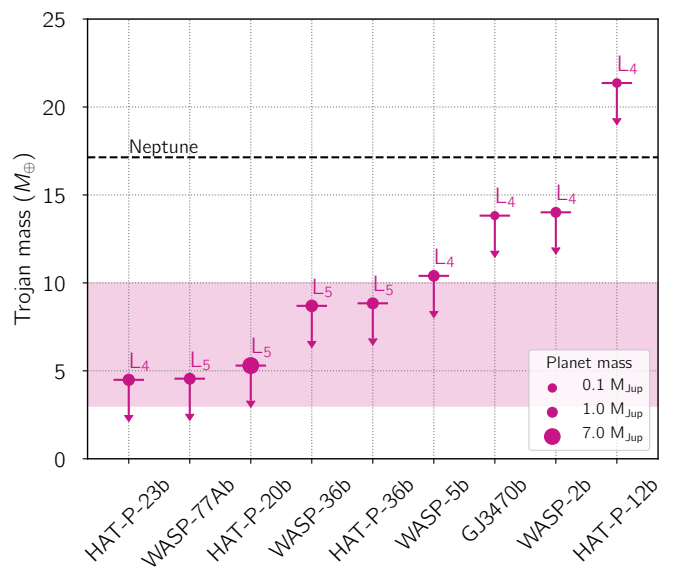


Fig. 8. Upper limits on the masses of trojan bodies located at the exact Lagrangian points of the nine systems studied. The symbol size scales as the mass of the planet. The mass of Neptune is marked for reference and the shaded regions represents the super-Earth mass regime.

(see § 3.2.2). In this case, we can neglect trojans larger than $5 R_\oplus$ with libration amplitudes smaller than 25° in the case of circular orbit for the trojan (otherwise they would have been detected in our data). If we assume non-zero eccentricity for the trojan, Fig. 7 shows how our observations constrain this eccentricity as a function of the libration amplitude. In a nutshell, only a highly eccentric orbit would allow small libration amplitudes.

The combination of the four epochs acquired for this target provides an upper limit for a trojan orbiting at the exact Lagrangian point of $1.39 R_\oplus$. The combination of all three techniques discards trojans with masses larger than $4 M_\oplus$ at the exact position of the L_4 Lagrangian point. Trojans up to $\sim 30 M_\oplus$ with moderate libration amplitudes ($\zeta < 25^\circ$) are still not rejected by our observations.

5. Discussion and conclusions

We have used information from the radial velocity, transit and TTVs techniques to constrain the presence of co-orbital bodies in nine planetary systems previously showing hints for their presence (Lillo-Box et al. 2018a). These systems correspond to short-period ($P < 5$ days) mainly massive planets, where high-precision measurements from the three techniques can be obtained and found in the archive. The three techniques complement each other in the parameter space composed by the trojan mass versus libration amplitude, allowing us to progressively discard trojans at different regimes.

For instance, in Fig. 8, we show the upper mass limits for co-orbitals exactly at the Lagrangian points of eight of the studied systems combining all three techniques. As we can see, we can discard trojans more massive than $10 M_\oplus$ in six of the systems and we can go down to $5 M_\oplus$ regime in the case of HAT-P-23, WASP-77A, and HAT-P-20. The key observations in these three systems have been the combination of more than three transit observations of the Lagrangian passage with photometric precisions at the ~ 1 mmag level with CAFOS and WiFSIP. In the case of WASP-5, the key technique was the radial velocity follow-up

with HARPS combined with the accurate measurements of the planet's mid-transit time and mid secondary eclipse time (breaking the degeneracy with the eccentricity).

We here show that ground-based photometric exploration of the Lagrangian points of known planets can provide constraints on trojan bodies in these regions down to the Earth-size regime when combining > 3 epochs with mmag precision for solar-like stars. It is important to note that intensive ground-based monitoring from small robotic telescopes would strongly increase the sample of explored systems in an efficient way.

The exploration of Kepler/K2 data was partly done by Janson (2013) with no positive detections. However, Hippke & Angerhausen (2015) found clear dims at L_4 and L_5 of the combined Kepler light curve obtained by stacking all planet candidates, showing that on average all Kepler planets have co-orbitals of few hundreds of kilometers size (or equivalently swarms of small trojans with an equivalent cross-section of this size). Hence, a dedicated exploration of this data (taking into account possible large libration amplitudes) should reveal the presence of the individual co-orbitals (Lillo-Box et al., 2018c, in prep.). In the future, TESS photometry (Ricker et al. 2014) will also help to find these bodies in many systems with precisions similar to Kepler and a 2-min cadence for many of them, which is critical in case of large libration amplitudes. Additionally, the CHEOPS mission (Broeg et al. 2013) will be a unique opportunity to follow-up best candidates, reaching lower trojan radii down to the rocky regime.

Acknowledgements. We thank Mathias Zechmeister for his useful advice and support with the SERVAL pipeline for CARMENES, which is partly used in our new pipeline to obtain the RVs with the CCF technique (carmeneX). J.L.-B acknowledges financial support from the European Southern Observatory (ESO). Parts of this work have been carried out within the frame of the National Centre for Competence in Research PlanetS supported by the SNSF. DB acknowledges financial support from the Spanish grant ESP2015-65712-C5-1-R. NCS, PF and JF were supported by Fundação para a Ciência e a Tecnologia (FCT, Portugal) through the research grant through national funds and by FEDER through COMPETE2020 by grant PTDC/FIS-AST/1526/2014 & POCI-01-0145-FEDER-016886, as well as through Investigador FCT contracts nr. IF/01037/2013CP1191/CT0001 and IF/00169/2012/CP0150/CT0002. J.J.N. also acknowledges support from FCT through the PhD:Space fellowship PD/BD/52700/2014. A.C. acknowledges support from CIDMA strategic project (UID/MAT/04106/2013), ENGAGE SKA (POCI-01-0145-FEDER-022217), and PHOBOS (POCI-01-0145-FEDER-029932), funded by COMPETE 2020 and FCT, Portugal. H.P. has received support from the Leverhulme Research Project grant RPG-2012-661.

References

- Aceituno, J., Sánchez, S. F., Grupp, F., et al. 2013, *A&A*, 552, A31
 Appenzeller, I. & Rupprecht, G. 1992, *The Messenger*, 67, 18
 Astropy Collaboration, Robitaille, T. P., Tollerud, E. J., et al. 2013, *A&A*, 558, A33
 Awiphan, S., Kerins, E., Pichadee, S., et al. 2016, *MNRAS*, 463, 2574
 Bakos, G. Á., Hartman, J., Torres, G., et al. 2011, *ApJ*, 742, 116
 Bakos, G. Á., Hartman, J. D., Torres, G., et al. 2012, *AJ*, 144, 19
 Baranne, A., Queloz, D., Mayor, M., et al. 1996, *A&AS*, 119, 373
 Bastürk, O., Hinse, T. C., Özavcainodot, et al. 2015, in *Astronomical Society of the Pacific Conference Series*, Vol. 496, *Living Together: Planets, Host Stars and Binaries*, ed. S. M. Rucinski, G. Torres, & M. Zejda, 370
 Beaugé, C., Sándor, Z., Érdi, B., & Süli, Á. 2007, *A&A*, 463, 359
 Bertin, E. & Arnouts, S. 1996, *A&AS*, 117, 393
 Bonfils, X., Gillon, M., Udry, S., et al. 2012, *A&A*, 546, A27
 Borisov, G., Christou, A., Bagnulo, S., et al. 2017, *MNRAS*, 466, 489
 Bradley, L., Sipocz, B., Robitaille, T., et al. 2017, *astropy/photutils: v0.4*
 Broeg, C., Fortier, A., Ehrenreich, D., et al. 2013, in *European Physical Journal Web of Conferences*, Vol. 47, *European Physical Journal Web of Conferences*, 3005
 Caballero, J. A., Guàrdia, J., López del Fresno, M., et al. 2016, in *Proc. SPIE*, Vol. 9910, *Observatory Operations: Strategies, Processes, and Systems VI*, 99100E
 Charbonneau, D., Winn, J. N., Everett, M. E., et al. 2007, *ApJ*, 658, 1322
 Chen, J. & Kipping, D. 2017, *ApJ*, 834, 17
 Collier Cameron, A., Bouchy, F., Hébrard, G., et al. 2007, *MNRAS*, 375, 951
 Cosentino, R., Lovis, C., Pepe, F., et al. 2012, in *Society of Photo-Optical Instrumentation Engineers (SPIE) Conference Series*, Vol. 8446, 1
 Faria, J. P., Haywood, R. D., Brewer, B. J., et al. 2016, *A&A*, 588, A31
 Ford, E. B. & Gaudi, B. S. 2006, *The Astrophysical Journal*, 652, L137
 Ford, E. B. & Holman, M. J. 2007, *ApJ*, 664, L51
 Foreman-Mackey, D., Hogg, D. W., Lang, D., & Goodman, J. 2013, *PASP*, 125, 306
 Fuente, A., Baruteau, C., Neri, R., et al. 2017, *ApJ*, 846, L3
 Granata, V., Nascimbeni, V., Piotto, G., et al. 2014, *Astronomische Nachrichten*, 335, 797
 Hartman, J. D., Bakos, G. Á., Torres, G., et al. 2009, *ApJ*, 706, 785
 Hippke, M. & Angerhausen, D. 2015, *ApJ*, 811, 1
 Hoyer, S., Hamman, J., Fitzgerald, C., et al. 2017, *pydata/xarray: v0.10.0*
 Hoyer, S., Rojo, P., & López-Morales, M. 2012, *ApJ*, 748, 22
 Hrudková, M., Skillen, I., Benn, C., et al. 2009, in *IAU Symposium*, Vol. 253, *Transiting Planets*, ed. F. Pont, D. Sasselov, & M. J. Holman, 446–449
 Janson, 2013, *ApJ*, 774, 156
 Kreidberg, L. 2015, *PASP*, 127, 1161
 Laughlin, G., Chambers, J., & Fischer, D. 2002, *ApJ*, 579, 455
 Laughlin, G. & Chambers, J. E. 2002, *Astronomical Journal*, 124, 592
 Lee, J. W., Youn, J.-H., Kim, S.-L., Lee, C.-U., & Hinse, T. C. 2012, *AJ*, 143, 95
 Leleu, A., Robutel, P., & Correia, A. C. M. 2015, *A&A*, 581, A128
 Leleu, A., Robutel, P., Correia, A. C. M., & Lillo-Box, J. 2017, *A&A*, 599, L7
 Levison, H., Olkin, C., Noll, K., & Marchi, S. 2017, *European Planetary Science Congress*, 11, EPSC2017
 Lillo-Box, J., Barrado, D., Figueira, P., et al. 2018a, *A&A*, 609, A96
 Lillo-Box, J., Barrado, D., Santos, N. C., et al. 2015, *A&A*, 577, A105
 Lillo-Box, J., Kipping, D., Rebollido, I., et al. 2018b, *ArXiv e-prints*, arXiv:1803.04010
 Madhusudhan, N. & Winn, J. N. 2009, *ApJ*, 693, 784
 Mallonn, M., Bernt, I., Herrero, E., et al. 2016, *MNRAS*, 463, 604
 Mallonn, M., Nascimbeni, V., Weingrill, J., et al. 2015, *A&A*, 583, A138
 Mancini, L., Lillo-Box, J., Southworth, J., et al. 2016, *A&A*, 590, A112
 Maxted, P. F. L., Anderson, D. R., Collier Cameron, A., et al. 2013, *PASP*, 125, 48
 Mayor, M., Pepe, F., Queloz, D., et al. 2003, *The Messenger*, 114, 20
 Meisenheimer, K. 1994, *Sterne und Weltraum*, 33, 516
 Morbidelli, A., Levison, H. F., Tsiganis, K., & Gomes, R. 2005, *Nature*, 435, 462
 Murray, C. D. & Correia, A. C. M. 2010, *Keplerian Orbits and Dynamics of Exoplanets*, ed. S. Seager, 15–23
 Namouni, F. & Morais, H. 2017, *ArXiv e-prints*, arXiv:1704.00550
 Pepe, F., Mayor, M., Galland, F., et al. 2002, *A&A*, 388, 632
 Perrakis, K., Ntzoufras, I., & Tsonas, E. G. 2014, *Computational Statistics & Data Analysis*, 77, 54
 Poddany, S., Brát, L., & Pejcha, O. 2010, *New A*, 15, 297
 Quirrenbach, A., Amado, P. J., Caballero, J. A., et al. 2014, in *Society of Photo-Optical Instrumentation Engineers (SPIE) Conference Series*, Vol. 9147, *Society of Photo-Optical Instrumentation Engineers (SPIE) Conference Series*, 1
 Ricker, G. R., Winn, J. N., Vanderspek, R., et al. 2014, in *Society of Photo-Optical Instrumentation Engineers (SPIE) Conference Series*, Vol. 9143, *Society of Photo-Optical Instrumentation Engineers (SPIE) Conference Series*, 20
 Rodríguez, A., Giuppone, C. A., & Michtchenko, T. A. 2013, *Celestial Mechanics and Dynamical Astronomy*, 117, 59
 Schwarz, R., Bzszó, Á., Funk, B., & Zechner, R. 2016, *arXiv.org*, arXiv:1608.00784
 Seabold, S. & Perktold, J. 2010, in *9th Python in Science Conference*
 Smith, A. M. S., Anderson, D. R., Collier Cameron, A., et al. 2012, *AJ*, 143, 81
 Southworth, J., Mancini, L., Novati, S. C., et al. 2010, *MNRAS*, 408, 1680
 Strassmeier, K. G., Granzer, T., Weber, M., et al. 2010, *Advances in Astronomy*, 2010, 970306
 Sun, L., Gu, S., Wang, X., et al. 2017, *AJ*, 153, 28
 van der Walt, S., Colbert, S. C., & Varoquaux, G. 2011, *Comput. Sci. Eng.*, 13, 22
 Zechmeister, M., Reiners, A., Amado, P. J., et al. 2018, *A&A*, 609, A12

Appendix A: Figures**Table B.1.** New radial velocities obtained for GJ 3470.

Julian date	RV (km/s)	σ_{RV} (km/s)	Instrument
2457791.50172	26.5240	0.0029	HARPS-N
2457791.58217	26.5266	0.0025	HARPS-N
2457792.36992	26.5200	0.0023	HARPS-N
2457792.55721	26.5118	0.0022	HARPS-N
2457793.40268	26.5123	0.0032	HARPS-N
2457793.53939	26.5186	0.0023	HARPS-N

Table B.2. New radial velocities obtained for HAT-P-12.

Julian date	RV (km/s)	σ_{RV} (km/s)	Instrument
2457784.64979	-41.1009	0.0026	CARMENES
2457784.75095	-41.0845	0.0023	CARMENES
2457785.63389	-41.0332	0.0045	CARMENES
2457785.73902	-41.0413	0.0039	CARMENES
2457785.76369	-41.0403	0.0037	CARMENES
2457791.66003	-40.4358	0.0067	HARPS-N
2457791.72821	-40.4217	0.0065	HARPS-N
2457792.67559	-40.4414	0.0051	HARPS-N
2457792.76510	-40.4491	0.0039	HARPS-N
2457793.68221	-40.4957	0.0050	HARPS-N
2457793.77300	-40.4957	0.0044	HARPS-N

Appendix B: Tables

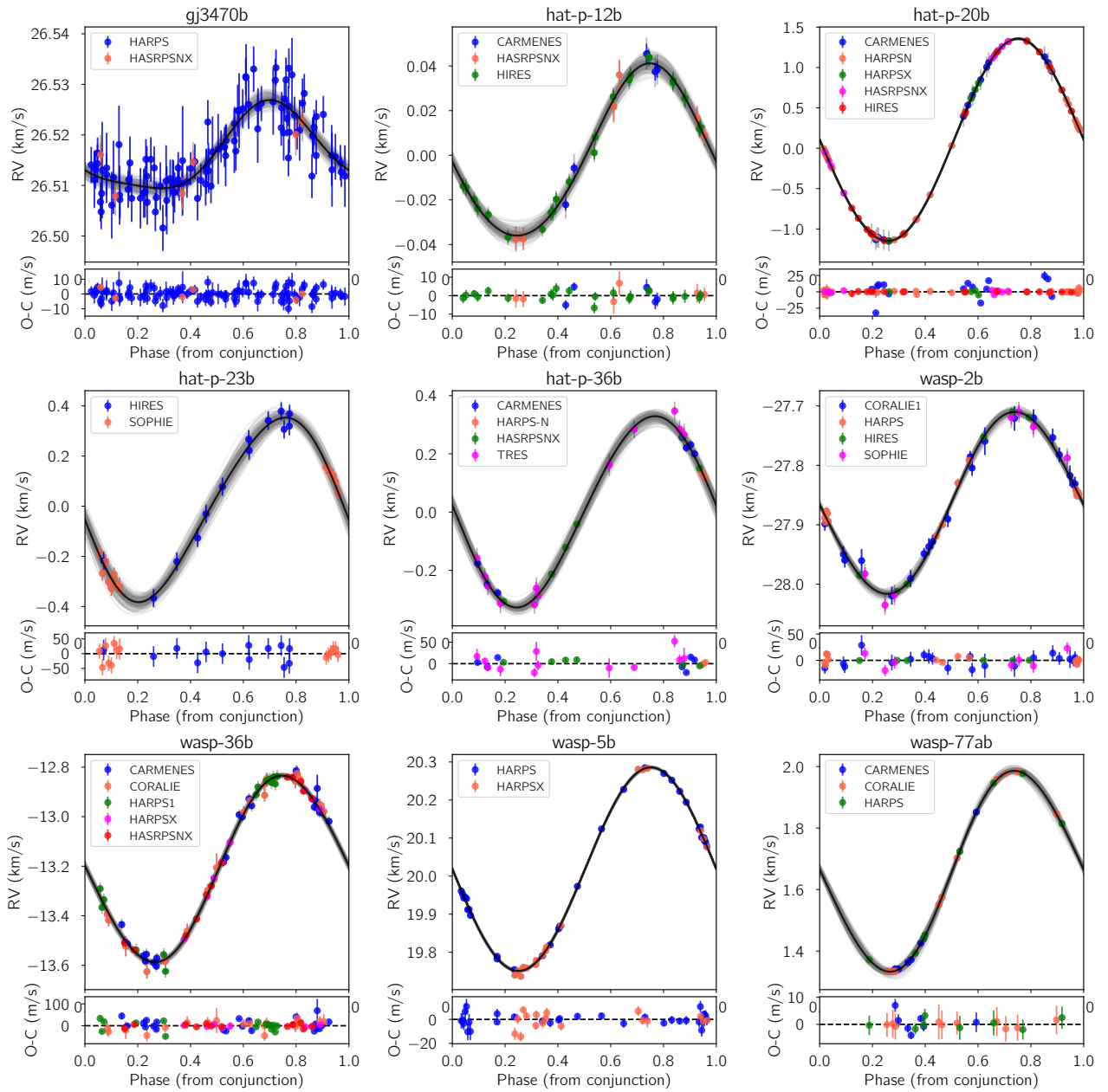


Fig. A.1. Radial velocity analysis of the nine studied systems. The colors of the symbols represent the instrument used, with HARPSN being HARPS-N data from archive, HARPSNX and HARPSX being newly acquired data with HARPS-N and HARPS (respectively) in the context of *TROY* project. All CARMENES data were also obtained for this project.

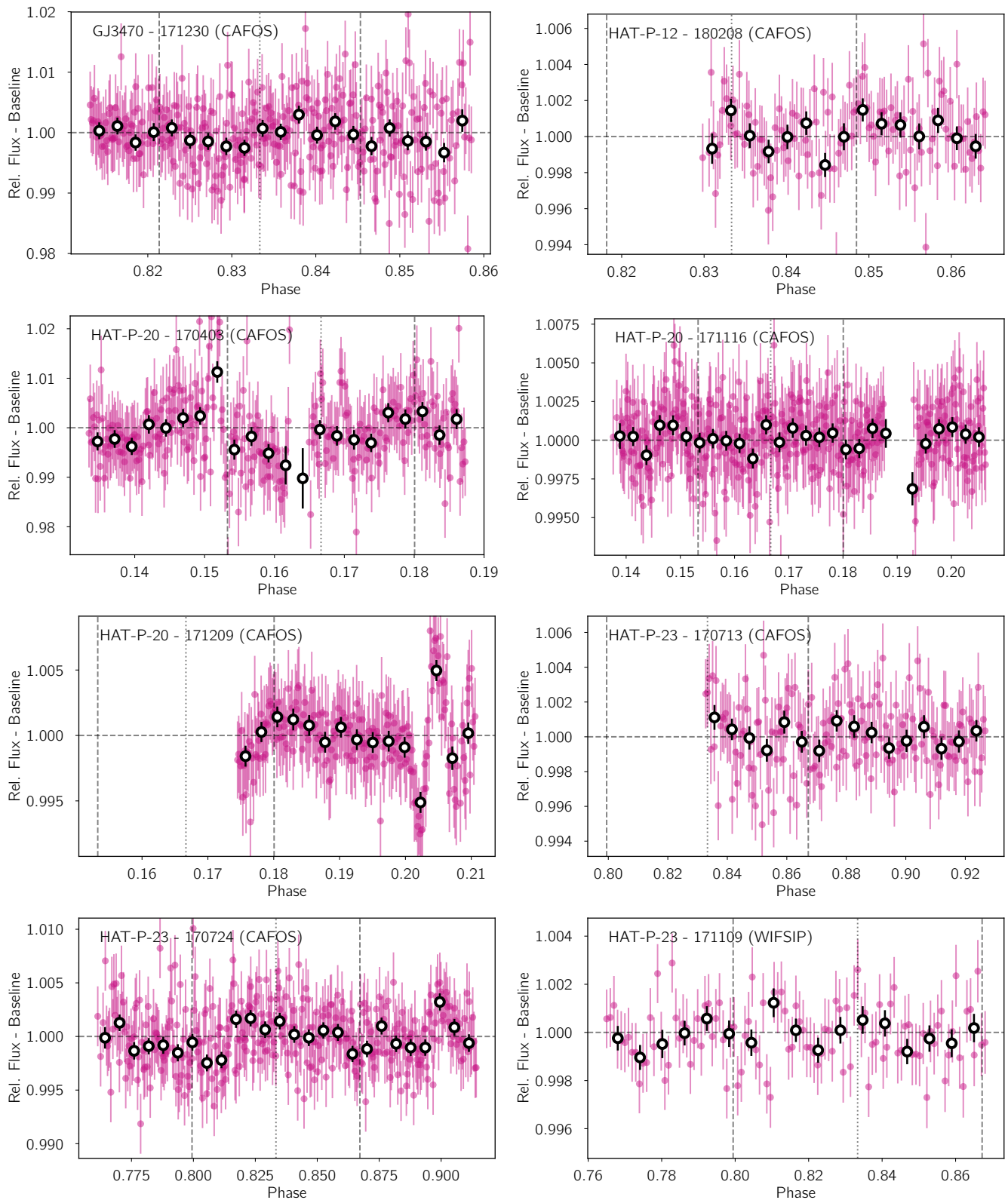


Fig. A.2. Light curves of all Lagrangian point transits observed with ground-based facilities. A linear baseline model accounting for time, seeing, airmass, XY positions on the detector, and background has been removed. Purple data points are the individual measurements while big black open symbols represent 10-minute bins. The system and observing date (in YYMMDD format) are shown in each panel. The vertical dashed line indicates the mid-transit passage of the Lagrangian point and the dotted vertical lines indicate the total duration of the transit assuming the same as the planet.

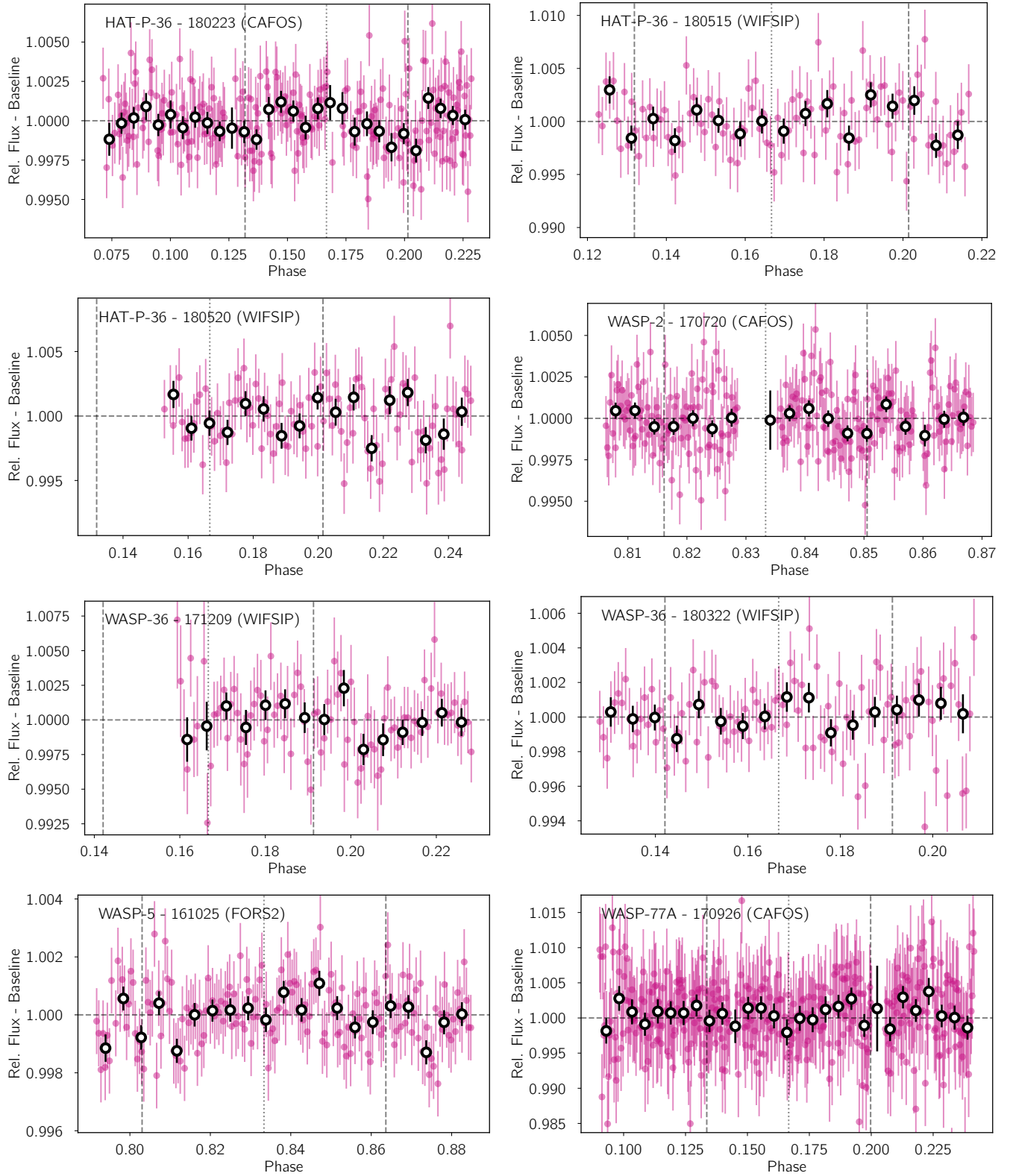


Fig. A.3. Continuation of Fig A.2.

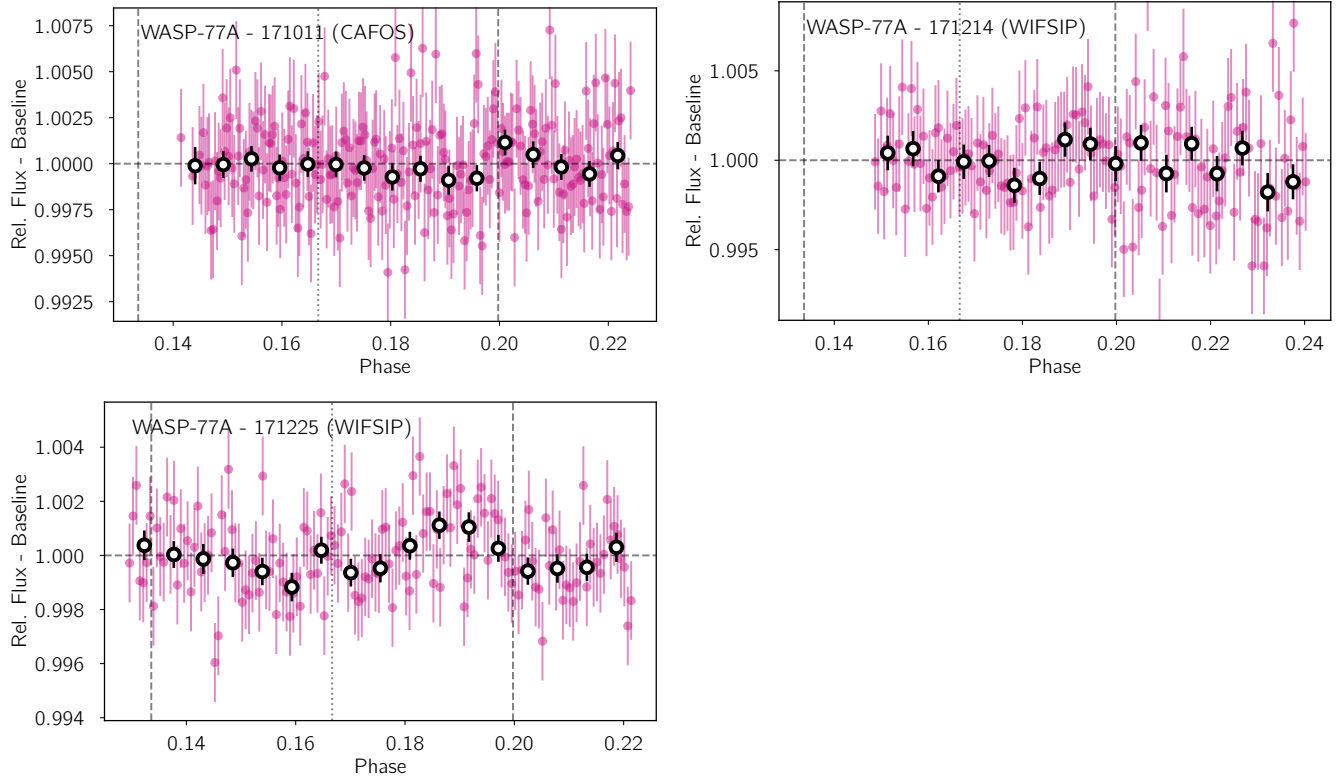


Fig. A.4. Continuation of Fig A.2.

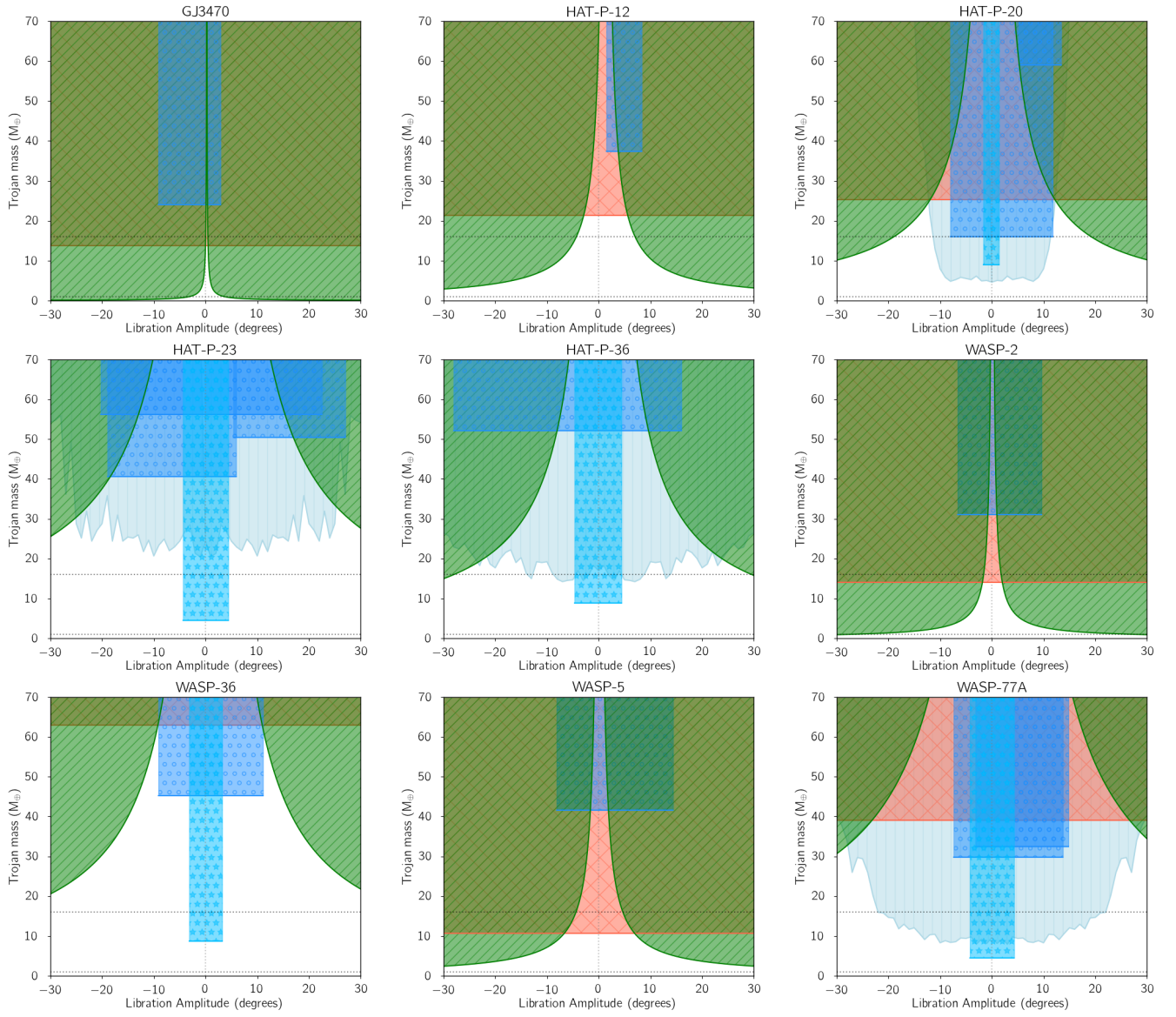


Fig. A.5. Constrain of the trojan mass versus libration amplitude parameter space based on the three techniques used in this paper. The constrain from individual transits is shown as blue shaded regions with open circles, the constrain from the combined light curve is shown in light blue with open star symbols, the constrain from TTVs is shown as green diagonally striped shaded region, and the RV constrain is shown as a red vertically striped shaded region. The two horizontal dotted lines represent the Earth and Neptune and are shown to guide the eye.

Table B.3. New radial velocities obtained for HAT-P-20.

Julian date	RV (km/s)	σ_{RV} (km/s)	Instrument
2457778.73074	-19.3379	0.0030	HARPS
2457779.62713	-17.5785	0.0021	HARPS
2457779.66825	-17.4749	0.0020	HARPS
2457779.70548	-17.3942	0.0029	HARPS
2457783.29928	-17.3966	0.0071	CARMENES
2457783.33735	-17.4780	0.0028	CARMENES
2457783.37978	-17.6001	0.0017	CARMENES
2457784.29131	-19.8829	0.0014	CARMENES
2457784.33715	-19.9465	0.0017	CARMENES
2457784.35189	-19.9118	0.0017	CARMENES
2457784.36669	-19.9133	0.0019	CARMENES
2457784.42444	-19.9156	0.0016	CARMENES
2457784.47847	-19.9112	0.0011	CARMENES
2457785.29185	-18.1693	0.0021	CARMENES
2457785.33989	-18.0342	0.0019	CARMENES
2457785.39013	-17.9107	0.0026	CARMENES
2457785.47954	-17.7162	0.0011	CARMENES
2457785.54400	-17.5504	0.0018	CARMENES
2457785.56634	-17.4910	0.0014	CARMENES
2457791.35401	-17.0477	0.0024	HARPS-N
2457791.37720	-17.0165	0.0025	HARPS-N
2457791.41835	-16.9499	0.0025	HARPS-N
2457791.46151	-16.8990	0.0020	HARPS-N
2457791.52634	-16.8384	0.0025	HARPS-N
2457792.40987	-18.2047	0.0017	HARPS-N
2457792.45106	-18.3115	0.0019	HARPS-N
2457792.47385	-18.3708	0.0021	HARPS-N
2457792.61402	-18.7004	0.0024	HARPS-N

Table B.4. New radial velocities obtained for HAT-P-36.

Julian date	RV (km/s)	σ_{RV} (km/s)	Instrument
2457784.62650	-17.0151	0.0024	CARMENES
2457784.67574	-17.0888	0.0020	CARMENES
2457784.72818	-17.1169	0.0021	CARMENES
2457785.65525	-16.5881	0.0025	CARMENES
2457785.67649	-16.6234	0.0028	CARMENES
2457785.69869	-16.6133	0.0037	CARMENES
2457785.71784	-16.6445	0.0038	CARMENES
2457791.63596	-16.5054	0.0052	HARPS-N
2457791.70608	-16.4135	0.0057	HARPS-N
2457791.76242	-16.3341	0.0058	HARPS-N
2457792.72138	-16.5978	0.0037	HARPS-N
2457793.62341	-16.0329	0.0032	HARPS-N
2457793.70754	-16.1395	0.0035	HARPS-N
2457793.75023	-16.2006	0.0028	HARPS-N

Table B.5. New radial velocities obtained for WASP-5.

Julian date	RV (km/s)	σ_{RV} (km/s)	Instrument
2457673.57366	19.7310	0.0051	HARPS
2457673.59153	19.7426	0.0042	HARPS
2457673.61023	19.7280	0.0040	HARPS
2457673.62602	19.7517	0.0029	HARPS
2457673.64561	19.7499	0.0028	HARPS
2457709.53130	19.7889	0.0034	HARPS
2457709.58860	19.8153	0.0029	HARPS
2457709.68416	19.8803	0.0036	HARPS
2457710.54488	20.1298	0.0021	HARPS
2457710.56189	20.1091	0.0022	HARPS
2457710.58478	20.0869	0.0020	HARPS
2457710.60295	20.0778	0.0022	HARPS
2457765.52618	20.2705	0.0040	HARPS
2457765.55328	20.2697	0.0038	HARPS
2457765.58348	20.2734	0.0054	HARPS
2457766.52305	19.7537	0.0033	HARPS
2457766.56604	19.7764	0.0040	HARPS
2457766.59011	19.7991	0.0043	HARPS

Table B.6. New radial velocities obtained for WASP-77 A.

Julian date	RV (km/s)	σ_{RV} (km/s)	Instrument
2458100.35100	1.3746	0.0036	CARMENES
2458101.29327	0.8239	0.0024	CARMENES
2458101.30958	0.8209	0.0023	CARMENES
2458101.35856	0.8380	0.0016	CARMENES
2458101.37478	0.8458	0.0014	CARMENES
2458101.42477	0.8961	0.0011	CARMENES
2458101.44026	0.9101	0.0013	CARMENES

Table B.7. New radial velocities obtained for WASP-36.

Julian date	RV (km/s)	σ_{RV} (km/s)	Instrument
2457778.76807	-12.8833	0.0107	HARPS
2457778.80797	-12.9182	0.0068	HARPS
2457778.85385	-12.9576	0.0069	HARPS
2457779.60030	-13.4827	0.0061	HARPS
2457779.73384	-13.3094	0.0088	HARPS
2457779.77421	-13.2352	0.0070	HARPS
2457779.82374	-13.1700	0.0108	HARPS
2457779.86853	-13.0910	0.0177	HARPS
2457783.44083	-13.5112	0.0146	CARMENES
2457783.45054	-13.4601	0.0542	CARMENES
2457784.44115	-13.7575	0.0061	CARMENES
2457784.45624	-13.7384	0.0057	CARMENES
2457784.53293	-13.5657	0.0051	CARMENES
2457784.55202	-13.5744	0.0057	CARMENES
2457784.59006	-13.5012	0.0103	CARMENES
2457784.60601	-13.5290	0.0120	CARMENES
2457785.41944	-14.0861	0.0106	CARMENES
2457785.52423	-14.1569	0.0052	CARMENES
2457785.59082	-14.1437	0.0071	CARMENES
2457791.55299	-13.4939	0.0096	HARPS-N
2457791.60835	-13.5219	0.0097	HARPS-N
2457792.50103	-12.8269	0.0059	HARPS-N
2457792.53141	-12.8277	0.0062	HARPS-N
2457792.57894	-12.8443	0.0102	HARPS-N
2457792.59412	-12.8832	0.0105	HARPS-N
2457792.64469	-12.9135	0.0087	HARPS-N
2457793.44677	-13.4685	0.0083	HARPS-N
2457793.50910	-13.4019	0.0060	HARPS-N
2457793.56663	-13.3037	0.0065	HARPS-N
2457793.59534	-13.2685	0.0060	HARPS-N
2457793.65484	-13.1750	0.0081	HARPS-N
2458100.54522	-14.0508	0.0137	CARMENES
2458100.56529	-14.1231	0.0129	CARMENES
2458100.67273	-14.1769	0.0106	CARMENES
2458100.68894	-14.1711	0.0117	CARMENES
2458100.73091	-14.2054	0.0104	CARMENES
2458100.74677	-14.2196	0.0101	CARMENES
2458101.54573	-13.4606	0.0078	CARMENES
2458101.56070	-13.4320	0.0078	CARMENES
2458101.66642	-13.5792	0.0060	CARMENES
2458101.68185	-13.5828	0.0054	CARMENES
2458101.69731	-13.6015	0.0053	CARMENES
2458101.71265	-13.6024	0.0060	CARMENES
2458101.75226	-13.6371	0.0069	CARMENES

Table B.8. Summary of photometric data obtained for the 10 systems analyzed in this paper.

System	Date	Instrument	Filter	Lpoint (L4/L5)	Coverage (phase)	Span (hours)	Texp (s)	#images	$\hat{\sigma}_{LC}^{(a)}$ (mmag)
GJ 3470	2017-dec-30	CAFOS	SDSSz	L4	0.813-0.859	3.63	2-20	330	0.93
HAT-P-12	2018-feb-08	CAFOS	SDSSi	L4	0.830-0.864	2.64	20-180	128	0.41
HAT-P-20	2017-apr-03	CAFOS	SDSSz	L5	0.133-0.187	3.72	5-20	298	0.97
	2017-nov-16	CAFOS	SDSSi	L5	0.138-0.206	4.74	4-8	399	0.42
	2017-dec-09	CAFOS	SDSSi	L5	0.175-0.211	2.50	5-9	210	0.38
HAT-P-23	2017-jul-13	CAFOS	SDSSz	L4	0.833-0.927	2.73	10-28	<67	0.44
	2017-jul-24	CAFOS	SDSSz	L4	0.761-0.914	4.45	7-16	351	0.49
	2017-nov-09	WiFSIP	rp	L4	0.766-0.869	3.0	60	105	0.31
HAT-P-36	2017-02-23	CAFOS	SDSSi	L5	0.064-0.256	5.00	10-38	231	0.50
	2018-05-15	WiFSIP	rp	L5	0.123-0.217	2.98	60	102	0.41
	2018-05-20	WiFSIP	rp	L5	0.064-0.256	2.99	10-38	104	0.40
WASP-2	2017-jul-20	CAFOS	SDSSi	L4	0.806-0.869	3.21	7-12	236	0.28
WASP-36	2017-dec-09	WiFSIP	rp	L5	0.159-0.228	2.54	60	88	0.76
	2018-jan-01	CAFOS	SDSSz	L5	0.128-0.209	2.99	25-60	101	0.46
WASP-5	2016-oct-26	FORS2	z_SPECIAL	L4	0.792-0.885	3.64	12	174	0.18
WASP-77	2017-sep-26	CAFOS	SDSSi	L5	0.090-0.241	4.93	4-12	376	0.80
	2017-oct-11	CAFOS	SDSSi	L5	0.141-0.224	2.70	5-13	228	0.40
	2017-dec-14	WiFSIP	rp	L5	0.149-0.240	2.99	10	145	0.26
	2017-dec-25	WiFSIP	rp	L5	0.130-0.221	3.0	10	148	0.24

Notes. ^(a) Mean uncertainty per 15-min bin.

Table B.9. Constraints for the transit time (phase in the case of the combined transits) and depth from the individual fitting to each epoch assuming no transit is found and a linear baseline model.

System	Date	Inst.	JD_in	JD_end	R_t^{\max}
			BJD-2457000 (days)		R_{\oplus}
GJ 3470	2017-dec-30	CAFOS	8118.5564	8118.6678	3.73
HAT-P-12	2018-feb-08	CAFOS	8158.6747	8158.7361	4.19
HAT-P-20	2017-apr-03	CAFOS	7847.3845	7847.5008	8.28
	2017-nov-16	CAFOS	8074.5465	8074.7055	2.94
	2017-dec-09	CAFOS	8097.6551	8097.7208	6.38
	Combined	-	0.140	0.200	2.02
HAT-P-23	2017-jul-13	CAFOS	7948.5736	7948.6464	5.78
	2017-jul-24	CAFOS	7959.4030	7959.5472	6.20
	2017-nov-09	WiFSIP	8067.3540	8067.4378	5.13
	Combined	-	0.775	0.925	1.39
HAT-P-36	2018-feb-23	CAFOS	8173.5360	8173.6985	5.97
	2018-may-15	WiFSIP	8254.5726	8254.6509	9.64
	2018-may-20	WiFSIP	8258.5943	8258.6731	13.3
	Combined	-	0.154	0.179	2.04
WASP-2	2017-jul-20	CAFOS	7955.5091	7955.6060	4.32
WASP-36	2017-dec-09	WiFSIP	8097.5313	8097.5992	8.02
	2018-mar-22	WiFSIP	8200.4865	8200.5731	5.44
	Combined	-	0.158	0.175	2.01
WASP-5	2016-oct-26	FORS2	7687.5323	7687.6344	5.15
WASP-77A	2017-sep-26	CAFOS	8023.5241	8023.6846	7.81
	2017-oct-11	CAFOS	8038.5539	8038.6216	4.48
	2017-dec-14	WiFSIP	8102.4852	8102.5647	7.06
	2017-dec-25	WiFSIP	8113.3395	8113.4193	4.27
	Combined	-	0.100	0.230	1.39